Journal of Molecular Structure 1380 (2027) 147405

Contents lists available at ScienceDirect

Journal of Molecular Structure

journal homepage: www.elsevier.com/locate/molstr

Nano route, DFT, MEP, and SAR of pyran-functionalized pyrimidinone hybrids as potent larvicides against *Culex pipiens*; biochemical and antioxidant assessments

Basant Farag [a,*], Mohamed Abdel-Haleem [b], Sampath Chinnam [c], Ismail A. Elhaty [d], Shaimaa Abozeid [e], Mohammed E. Gad [f], Aamer Saeed [g], Abdelfattah Selim [h], Mohamed M. Baz [i,j,*]

[a] Department of Chemistry, Faculty of Science, Zagazig University, Zagazig, 44519, Egypt
[b] Department of Botany and Microbiology, Faculty of Science, Zagazig University, Zagazig, 44519, Egypt
[c] Department of Chemistry, M.S. Ramaiah Institute of Technology (Autonoumous Institution, Affiliated to Visvesvaraya Technological University, Belgaum), Bengaluru, Karnataka, 560054, India
[d] Department of Nutrition and Dietetics, Faculty of Health Sciences, Istanbul Gelisim University, Istanbul, Turkey
[e] Entomology Department, Faculty of Science, Ain Shams University, Cairo, Abbassia, 11566, Egypt
[f] Department of Zoology and Entomology, Faculty of Science, Al Azhar University, Nasr City, Cairo, Egypt
[g] Department of Chemistry, Quaid-i-Azam University, Islamabad, 45320, Pakistan
[h] Department of Animal Medicine (Infectious Diseases), College of Veterinary Medicine, Benha University, Toukh, 13736, Egypt
[i] Department of Entomology, Faculty of Science, Benha University, Benha, 13518, Egypt
[j] Department of Biology, Faculty of Education and Arts, Sohar University, Sohar, 311, Oman

ARTICLE INFO

Keywords:
NPs
Pyran-pyrimidinone
Larvicides
Antioxidant
MEP
DFT
SAR

ABSTRACT

In this study, the starting material of the pyran-functionalized pyrimidinone scaffold was synthesized using nanoscience-based techniques. Larvicidal screening was conducted on 3rd larvae of *Culex pipiens*, the primary vector of West Nile virus according to standard protocols at various concentration levels. Among the synthesized library, derivative **11** emerged as the most potent candidate, displaying the strongest insecticidal power with the lowest LC_{50} values of 103.19 μg/mL after 24 h and 76.29 μg/mL after 48 h, as well as LC_{90} values of 248.92 μg/mL after 24 h and 195.75 μg/mL after 48 h. Biochemical assays revealed that larvae treated with the most potent derivative, **11**, showed a notable decrease in important enzymatic activity in comparison to the control. Specifically, the most potent derivative, **11**, inhibited AChE activity by approximately 50% and significantly suppressed both *α*- and *β*-esterase levels at the LC_{50} concentration. The study found that treated larvae showed major decreases in both protease and phosphatase digestive enzymes, which resulted in metabolic and digestive process disruptions. The assays revealed that whereas antioxidant enzyme activity declined, lipid peroxidation and total protein carbonyl content increased, which indicated severe oxidative stress and cell damage. The synthesized compounds exhibited promising antioxidant activity, with compound **11** showing the highest radical scavenging potential among the tested derivatives (IC_{50} = 4.30 μg/mL), approaching the activity of the reference standard ascorbic acid (IC_{50} = 3.98 μg/mL). Computational DFT studies showed that the synthesized derivatives have moderate electronic stability, with compound **11** displaying the smallest HOMO-LUMO gap and highest softness. The most reactive sites were identified by Fukui, MEP, and Mulliken studies. According to findings, the synthesized compounds are promising bioactive candidates for developing effective multiple roles.

1. Introduction

The mosquito stands as one of the most significant insect species that transmits numerous human diseases across the globe, resulting in millions of annual cases [1]. The genus *Culex* holds special significance in medicine because its species serve as disease carriers for West Nile fever,

* Corresponding authors.
E-mail addresses: basantfarag@zu.edu.eg (B. Farag), mahafez@zu.edu.eg (M. Abdel-Haleem), sampathchinnam@gmail.com (S. Chinnam), iaeismail@gelisim.edu.tr (I.A. Elhaty), asaeed@qau.edu.pk (A. Saeed), mohamed.albaz@fsc.bu.edu.eg (M.M. Baz).

https://doi.org/10.1016/j.molstruc.2026.147405
Received 19 July 2026; Received in revised form 20 August 2026; Accepted 21 August 2026
Available online 22 August 2026

Rift Valley fever, and lymphatic filariasis [2]. *Culex pipiens* has established its presence throughout urban and semi-urban areas because of its ability to adapt to various ecological conditions and breed in contaminated water sources [3]. In particular, *Cx. pipiens* is recognized as the primary vector of West Nile virus (WNV), a zoonotic pathogen that poses a significant public health threat in many regions, including Egypt. Controlling larval populations of this vector is a critical intervention point, as it directly interrupts the mosquito life cycle and reduces the emergence of adult females capable of transmitting WNV to susceptible hosts. Therefore, the development of effective larvicidal agents against *Cx. pipiens* is a key strategy for WNV disease prevention [4,5].

The ongoing distribution of this mosquito species, together with rising insecticide resistance rates, has created an urgent requirement for new larvicidal substances that function through different mechanisms. Chemical larvicides are one of the most effective ways to manage mosquito populations in control programs [6]. The excessive application of synthetic insecticides over extended periods has caused mosquito strains to become resistant, which diminishes the effectiveness of numerous chlorine products found in stores [7]. The body develops resistance in two ways, which include increased detoxification enzyme production and changes to insect body systems [8].

Despite the effectiveness of conventional insecticides, their widespread use has raised concerns about environmental pollution and their toxicity to non-target organisms. This study does not aim to address these environmental challenges directly but rather focuses on discovering novel chemical structures with potent larvicidal activity in vitro and elucidating their precise biochemical mechanisms of action. Assessing the environmental safety and toxicity of these synthesized compounds to non-target organisms requires separate and specialized studies beyond the scope of this initial chemical and biological screening [9]. The scientific community has turned its attention to research that seeks to discover new heterocyclic compounds that demonstrate better effective larvicidal properties while creating less environmental damage.

The scientific community has focused extensive research efforts on pyran-pyrimidinone derivatives because their research shows multiple biological functions, which range from antimicrobial activity to antioxidant activity and antitumor activity and insecticidal effects [10]. The majority of heterocycles have attracted attention in medicinal chemistry and account for numerous FDA-approved drugs [11,12]. Pyrimidine is a dinitrogen heterocyclic scaffold that possesses diverse biological effects such as anticancer, antimicrobial, antitubercular, and antioxidant [13,14]. 5-Flu shows structural resemblance to the pyrimidine scaffold. Among *O*-heterocycles, pyran is a versatile and studied pharmacophore due to its diverse pharmacological potential [15,16] (Fig. 1).

Research shows that structural changes to pyran-pyrimidinone scaffolds lead to better biological results because the new structures create stronger connections with different biological activities. Research studies have established that heterocyclic compounds that contain pyrimidinone rings produce strong insecticidal effects against mosquito larvae and other insect species [17]. Accordingly, the present study designed a series of pyran-functionalized pyrimidinone hybrids with varying substituents (e.g., carbamothiol group in compound **11** and hydrazonamide in compound **13**) to systematically explore how structural variation influences larvicidal activity and associated biochemical responses. The findings showed that pyran–pyrimidinone hybrid compounds may function as effective scaffolds for creating new mosquito larvicides.

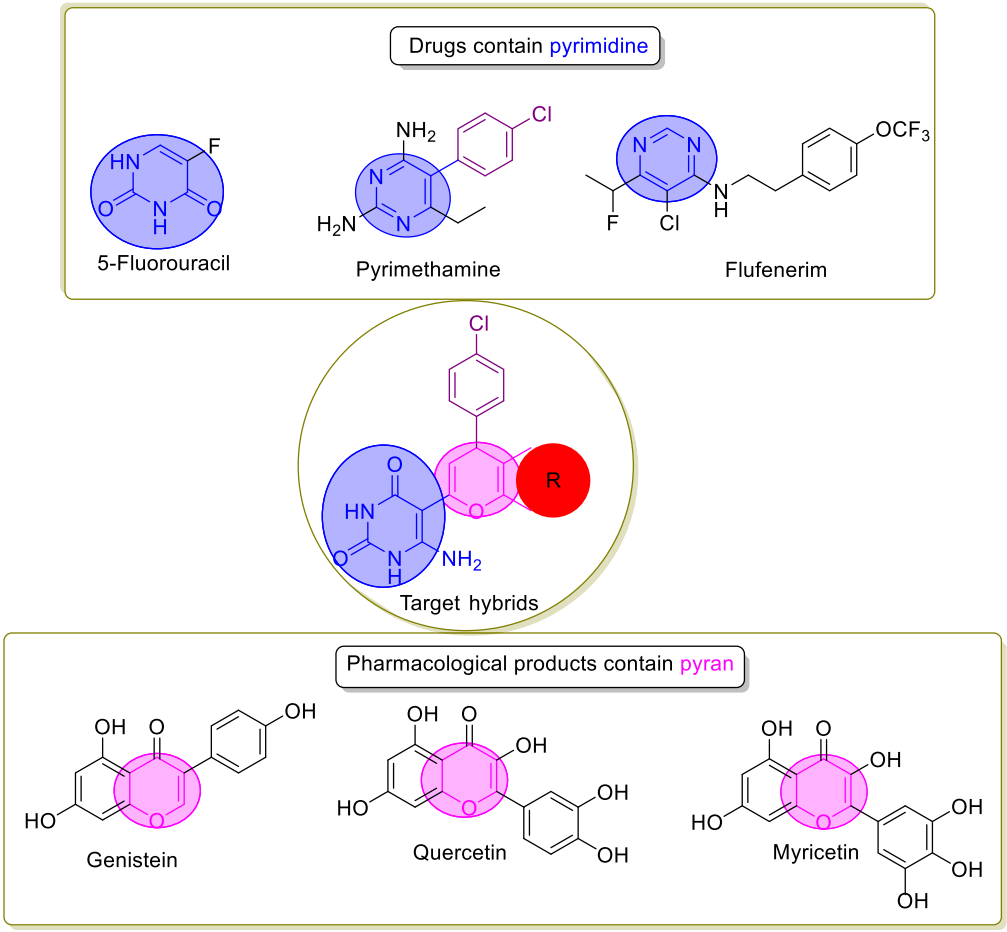

Fig. 1. Rational design of the target synthesized pyrimidine-linked pyran hybrids.

Mosquito control efforts should focus on the larval stage as the best target because larvae stay in water until they become adults, which allows them to contact dangerous substances directly [18].

The biochemical tests deliver critical data that reveals the body systems that drive the lethal effects of the pesticide. Acetylcholinesterase functions as a vital insect neurotransmission enzyme because it breaks down acetylcholine at synaptic junctions. The AChE enzyme becomes inhibited, which causes insects to experience nonstop nerve activity that leads to their paralysis and eventual death [8]. Insecticide metabolism and detoxification processes depend on esterase enzymes, which include α- and β-esterases. The insect detoxification system together with metabolic resistance mechanisms will show disruption through changes in enzyme activity patterns.

Insects depend on digestive enzymes because these enzymes control the process of nutrient digestion and energy burning, which is vital for their larval growth and development. Proteases together with phosphatases function as direct participants in the processes of protein breakdown and nutrient absorption and the control of metabolic activities. The decrease of digestive enzyme activity will disrupt body functioning, which leads to adverse effects on larval survival [19]. The study of digestive enzymes that respond to larvicidal treatments gives scientists crucial information about how the tested substances affect metabolic processes.

Oxidative stress serves as a principal toxicological pathway that emerges when insects come into contact with insecticides. Toxic compounds may stimulate excessive generation of reactive oxygen species (ROS), which causes oxidative damage to cellular lipids, proteins, and nucleic acids. The antioxidant defense enzymes superoxide dismutase (SOD) and catalase and glutathione S-transferase (GST) work to safeguard cells from oxidative damage through their function in controlling redox equilibrium [20]. The body faces higher lipid peroxidation and protein oxidation when these antioxidant systems become inactive, which leads to cellular damage and mortality in insects.

In vitro tests, such as the DPPH (2,2-diphenyl-1-picrylhydrazyl) radical scavenging, are frequently employed to evaluate antioxidant activity. These techniques are frequently employed in combination with phytochemical research to connect chemical composition with biological activity and offer important insights into the capacity of compounds to scavenge free radicals [21,22].

Also, the rationale of the current research is to use NPs for the optimization process, as presented in Fig. 2. The optimization process has grown remarkably alongside the advancements in nanotechnology [23]. Nanotechnology, especially in the form of nanocatalysts, has become a key tool for preparing heterocyclic compounds, which form the backbone of most modern drugs and many bioactive molecules.

Pyran-functionalized pyrimidinones are hybrid structures in which a pyran ring (or a pyran-bearing side chain) is attached to a pyrimidinone core, making them unique scaffolds in medicinal chemistry due to their tunable electronic characteristics, simplicity of derivatization, and broad spectrum of biological activities [24–26]. Accordingly, the current investigation sought to evaluate the larvicidal efficacy of designed pyran-pyrimidinone hybrid derivatives against 3rd instar larvae of *Culex pipiens*. The study further investigated the biochemical and oxidative stress responses induced by these compounds through determination of larval mortality, lethal concentration values, detoxification enzyme activities, digestive enzyme alterations, antioxidant defense biomarkers, and oxidative stress indicators. Additionally, computational investigations, such as Fukui function, HOMO-LUMO energy gaps, MEP surface mapping, and Mulliken charge distribution, were carried out to evaluate the electronic structure and local reactivity. Followed by structure–activity relationships (SAR), promising candidates with favorable pharmacokinetic behavior potential.

2. Results and discussion

2.1. Evaluation of Ag-NPs properties

2.1.1. XRD analysis

The XRD pattern validates the Ag-NPs' face-centred cubic structure. Silver metal four peaks with 2θ values of 38.29, 44.56, 64.82, and 77.44 degrees are caused by the silver planes (111), (200), (220), and (311). These peaks are marked as 1–4 in fig. S1 [27]. The diffractogram shows four additional peaks at 32.35 [partial oxidation of Ag-NPs is frequently the cause of reported cubic Ag_2O reflections], 46.38 [shows an oxide contribution and overlaps with metallic Ag (200) but is shifted], 54.03 [in line with the oxide phase], and 57.66 degrees [residual precursor]. It has been determined that these peaks are connected to silver nanoparticles.

2.1.2. FT-IR analysis

Using the Fourier transform, unique vibrational signals that clarify surface properties are seen in Fig. S2. Three separate peaks were visible

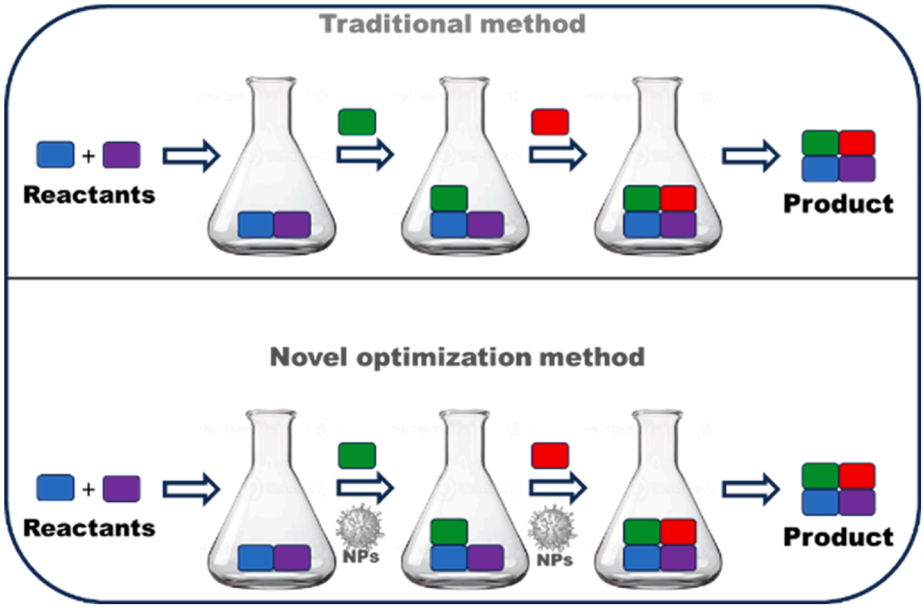

Fig. 2. Comparison of traditional synthesis and highlighting the novel optimization syn. method.

in the silver nanoparticles' FT-IR spectrum: 548.38, 1636.17, and 3347.85 cm^{-1}. The absorption band of amine is illustrated by the peak at 3347.85 cm^{-1} [28] whereas the C=O $_{amide}$ stretch vibration bond is responsible for the peak at 1636.17 cm^{-1} [29], and the fingerprint measures 548.38 cm^{-1}. Amino acid residues' carbonyl groups have a significant affinity for silver [30]. These spectroscopic findings clearly show that the nanoscale silver particles have increased surface reactivity [31].

2.1.3. SEM & EDX analyses

The visualization of Ag-NPs from scanning electron microscopy is displayed in Fig.S3(a) [32]. These findings demonstrated the formation of nanoclusters and spherical nanoparticles. Fig. S3(b) displays the elemental analysis data derived from energy-dispersive X-ray spectroscopy (EDX). The presence of Ag-NPs is confirmed by the silver peak at 3 eV [31].

2.1.4. TEM and SAED analyses

Fig. S4(a) displays the silver nanoparticles' TEM illustration. Using the X-ray diffraction pattern, it demonstrates that the particle size was approximately 15 nm, which is in line with the size of the crystallite [32]. Similarly, a technique used in TEM to determine the lattice parameters and crystallinity of nanoparticles from the diffraction pattern is called selected area electron diffraction. The majority of the particles' diameters fall within the 5 nm range, according to the matching histogram of silver nanoparticles in Fig. S4(b) [31].

2.1.5. Porosity characterization

Pore Size Distribution (BJH Model): The BJH curve of Ag nanopowder is displayed in Figure S5. Based on the peak area, the graphs indicate that most micropores are <40 nm, with a probable pore size of approximately 23 nm [33]. Mass transport in catalytic reactions is shown by the high pore volume.

2.2. Chemistry

Our literature reactions were optimized using a silver nanoparticle catalyst, as summarized in Table 1. We highlight that the benefits of our Ag-NP-assisted synthetic method go beyond quicker reaction times and greater yields in order to enhance its innovative nature. The Ag-NP catalytic role is proposed and rigorously demonstrated. We now present optimization studies that demonstrate how Ag-NP loadings affect reaction time and yield, showing the dependence of catalytic efficiency on nanoparticles. Reuse testing methods highlight the stability of Ag-NPs by showing that they maintain catalytic activity with no loss of performance. The technique was effectively scaled up from the millimole to the gram scale while keeping yield and selectivity, supporting its effectiveness. When taken as a whole, these findings offer both quantitative and qualitative support that the Ag-NPs function better than non-catalyzed pathways and behave as functional catalysts rather than just additives. In particular: Advantages of green chemistry Sustainable synthesis principles are in line with the milder circumstances in which reactions take place, minimizing the usage of harsh reagents and solvents. Among the optimization processes, hybrid **15** gave the highest yield (97.1%) in just 1.00 hour under reflux in formic acid. However, the optimization process for hybrid **13** also exhibited a shorter reaction time than reported in the literature, achieving a high yield (96.3%) under reflux conditions, which makes it a valuable and efficient optimization for this transformation. Also, literature hybrids **7, 11**, and **9**, respectively, exhibited shorter reaction times (4.00–2.15 h) and gave higher yields (95.9–93.8%), confirming the superior activity of the metal nanocatalyst, particularly Ag-NPs, in the optimization operation.

Table 1
Comparison between traditional literature and NPs' methodology for hybrids **5, 7, 9, 11, 13**, and **15**.

Traditional literature method [34]				NPs' Method		
Compound	**Time (h)**	**Yield (%)**	**YE**	**Time (h)**	**Yield (%)**	**YE**
5	24	86	3.58	6.00	94.5	15.7
7	10	86	8.60	2.15	95.9	44.6
9	20	88	4.40	4.00	93.8	23.4
11	17	88	5.17	3.45	94.5	27.3
13	6	83	13.8	2.00	96.3	48.1
15	10	93	9.30	1.00	97.1	97.1

Ag-NPs are thought to improve reaction efficiency mechanistically by adsorbing 4-chlorobenzylidenemalononitrile and 5-acetyl-6-aminouracil onto their surface, which facilitates nucleophilic attack and stabilizes the TS. The cyclization process is accelerated, and the activation energy is lowered by this surface-mediated interaction. As the final product desorbs from the surface of the nanoparticle, water is proposed to be produced as a byproduct (Scheme 1 & S1). Additionally, a remarkable 94.5% yield was produced in just 6 h as this process was modified utilizing Ag-NPs in normal conditions of reflux, demonstrating the great catalytic efficiency of the NPs system. Furthermore, three D_2O-exchangeable signals at δ 10.01, 10.57, and 10.64 ppm were identified for three secondary amines in the ^1H NMR of **5**. Five of the fifteen signals found in the ^{13}C NMR analysis of **5** are particularly at $\delta = 90.01$, 107.35, 129.43, 158.60, and 162.56 ppm with a relative pyran moiety. The mass spectrum of **5** showed a molecular ion peak at $m/z = 400$, confirming the proposed structure.

The reaction mechanism in the presence of Ag-NPs is proposed to proceed initially; Ag-NPs activate the cyano group of the starting material **5**, increasing the electrophilic character of the carbon center. This facilitates nucleophilic attack by ethyl cyanoacetate (**6**), yielding an α,β-imine intermediate, which undergoes a [1,3]-hydrogen shift to form the final scaffold system. Ag-NPs accelerate each step by providing a large surface area for efficient adsorption and reaction of the substrates, leading to high product yield in a relatively short time. Hybrid **7** is via adding the active methylene to the -CN moiety of **5** (Scheme 2 & S2), as demonstrated by spectroscopic evidence. The proposed structure was validated by a molecular ion peak at $m/z = 513$ in the mass spectrum of **7**.

The reaction mechanism in the presence of Ag-NPs is proposed to proceed through a multi-step cascade process involving condensation and the hydrolysis reaction Initially, Ag-NPs activate the electrophilic attack step, increasing the electrophilic character of the carbon center. This facilitates nucleophilic attack afford the final heterocyclic system (Scheme 3). Ag-NPs accelerate each step by providing a large surface area for efficient adsorption and reaction of the substrates, leading to high product yield in a relatively short time. The ^1H NMR spectrum of **9** illustrated two singlets attributed to two -NH_2 groups at δ 7.14 and 7.69 ppm. The ^{13}C NMR spectrum of **9** presented a relative carbonyl carbon of the amide group at $\delta = 155.59$ ppm. The proposed structure was proven by a molecular ion peak at $m/z = 443$ in the mass spectrum of **9**. Furthermore, the ^1H NMR spectrum of **11** showed two singlets attributed to two -NH_2 groups only at δ 7.81 and 8.18 ppm. The ^{13}C NMR spectrum of **11** revealed a relative -C=S group at $\delta = 163.28$ ppm. The mass spectrum of **11** showed a molecular ion peak at $m/z = 459$, supporting the proposed structure. Acetohydrazonamide **13** was produced by condensing **5** with hydrazine hydrate (**12**). The ^1H NMR spectrum of **13** showed D_2O exchangeable signals at 7.56 ppm for -NH_2 moieties. A molecular ion peak that matched the material's molecular weight was evident in its mass spectrum. Hydrolyzing the *N*-acetyl group of **5** to carbonitrile **15**. Compound **15**'s ^1H NMR revealed that the methyl moiety had vanished to a free -NH_2 moiety, and the mass spectrum revealed a parent ion peak at 358.

The reaction time and yield for hybrids **5, 7, 9, 11, 13**, and **15** are shown in Table 1. Alternatively, yield economy value (YE) is a characterization utilized to measure the effectiveness of a chemical reaction in terms of traditional literature and NPs' techniques of the same reaction producing the same desired product in an economically viable manner.

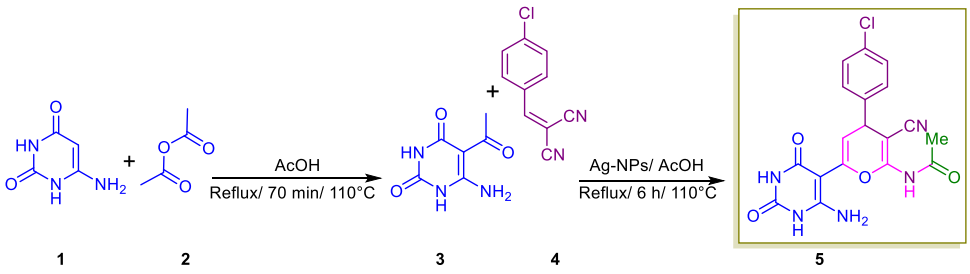

Scheme 1. Processes for the synthesis of the starting component **5** using Ag-NPs.

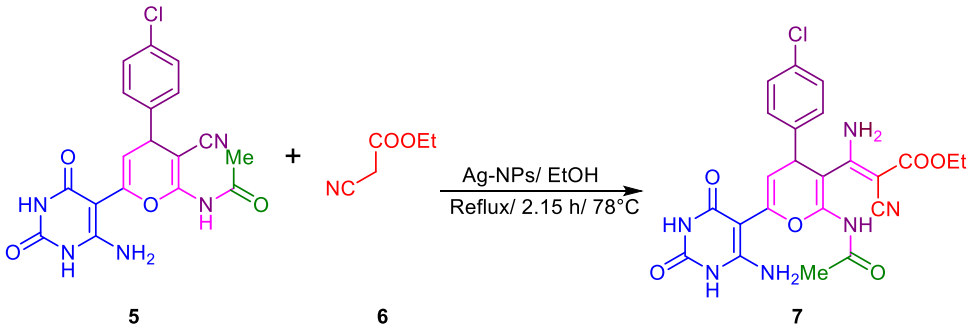

Scheme 2. Procedure for creating hybrid **7** using Ag-NPs.

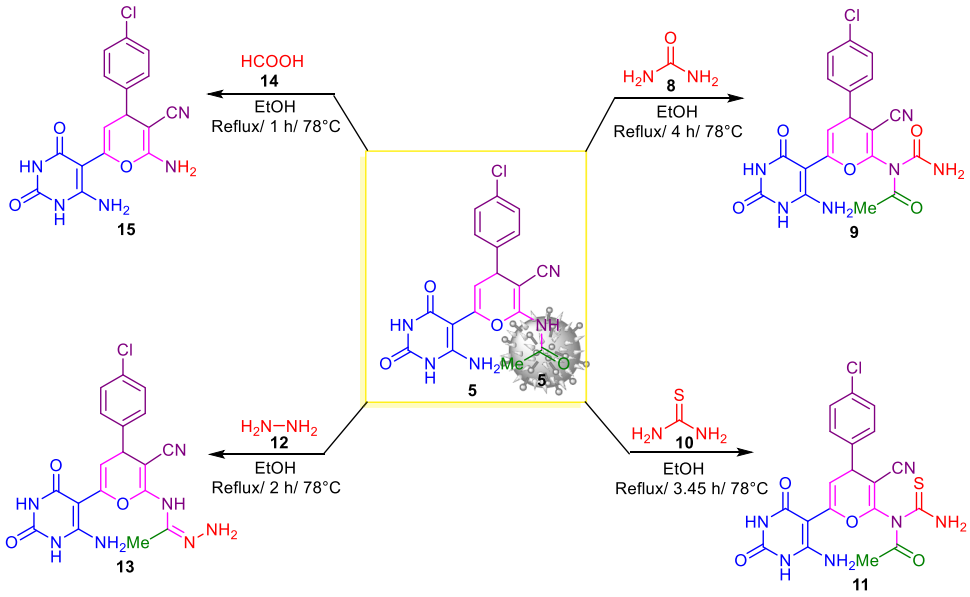

Scheme 3. Reaction. of *N*-(6-(3-cyano-4*H*-pyran-2-yl)acetamide **5** with urea (**8**), thiourea (**10**), hydrazine hydrate (**12**), and formic acid (**14**) for the formation of hybrids **9, 11, 13,** and **15**, respectively.

Eq. (1) was used to calculate YE [35,36].

$$YE = \frac{\text{Yield}}{\text{Reaction time}} \quad (1)$$

It is clear from an analysis of traditional literature and NPs' strategy method that the effectiveness of the NPs' method (15.7–97.1) significantly surpasses that of the traditional literature method (3.58–13.8), as illustrated in Table 1.

2.3. Biological studies

2.3.1. Larvicidal activity of pyran-pyrimidinone hybrids against culex pipiens

Pavela (2015) found that heterocyclic compounds with pyrimidinone-based structures showed increased insecticidal power after their functional groups underwent modification [17]. The larvicidal activity of the synthesized pyran-pyrimidinone hybrids was evaluated against 3rd instar larvae of *Culex pipiens* after 24 and 48 h of exposure. The experiments showed that every tested substance showed an increase in larvicidal effect as researchers increased its concentration. The results showed that larval death rates increased when researchers used greater concentrations and extended periods of exposure to test the

substances (Table 2). The study showed that mortality rates reached 100% at greater concentrations, which ranged from 500 to 1000 μg/mL, while lower concentrations between 25 and 50 μg per milliliter produced only minimal effects.

The larvicidal screening of pyran-pyrimidinone hybrids against *Cx. pipiens* revealed significant variations in toxicity, characterized by both concentration- and time-dependent effects (Fig. 3). Among the tested library, compound **11** emerged as the most potent derivative; at 24 h post-treatment, it achieved a mortality rate of 48.33% at 125 μg/mL, reaching total mortality (100%) at 500 μg/mL with a corresponding LC_{50} of 103.19 μg/mL (Table 2). Its efficacy further intensified after 48 h, recording 96.67% mortality at only 250 μg/mL and a reduced LC_{50} value of 76.29 μg/mL, confirming its superior insecticidal potential.

In contrast, compound **15** exhibited the lowest larvicidal activity, as evidenced by its higher LC_{50} values of 252.81 μg/mL and 193.57 μg/mL at 24 and 48 h, respectively. Meanwhile, compound **7** showed intermediate effectiveness, requiring a concentration of 1000 μg/mL to achieve complete larval death (Table 3). The consistent decline in lethal concentration values (LC_{50}, LC_{90}, and LC_{95}) across all compounds over the 48-hour period underscores a clear cumulative toxic effect, establishing these hybrids as promising candidates for mosquito vector control.

The research showed that pyran-pyrimidinone hybrid compounds, which researchers created, produced strong larvicidal effects against *Culex pipiens* larvae, but their effectiveness changed with different chemical structures and varying concentrations. The compound **11** showed the highest effectiveness against larvae among all tested compounds because its LC_{50} and LC_{90} values proved lower than those of other derivatives. The study produced LC_{50} values, which ranged from 76 to 252 μg/mL depending on the compound and exposure time, which showed strong toxicity toward synthetic heterocyclic larvicides that usually demonstrate LC_{50} values above 100 to 300 μg/mL under similar laboratory conditions [17]. Previous research on mosquito larvicidal studies demonstrated that extended exposure to active compounds led to cumulative toxic effects, which resulted in higher rates of larval mortality [37]. The epidemiological significance of targeting *Cx. pipiens* larvae lies in the fact that this species is the principal vector of West Nile virus (WNV) in Egypt and neighbouring regions [2]. Adult female mosquitoes acquire the virus through feeding on infected birds and subsequently transmit it to humans and other mammals during subsequent blood meals. By effectively reducing larval populations in their aquatic breeding habitats, larvicidal compounds such as the pyran-pyrimidinone hybrids tested in this study can significantly lower adult vector densities, thereby reducing the risk of WNV transmission. This vector-targeted approach aligns with integrated vector management (IVM) strategies recommended by the World Health Organization for mosquito-borne disease control [38] .

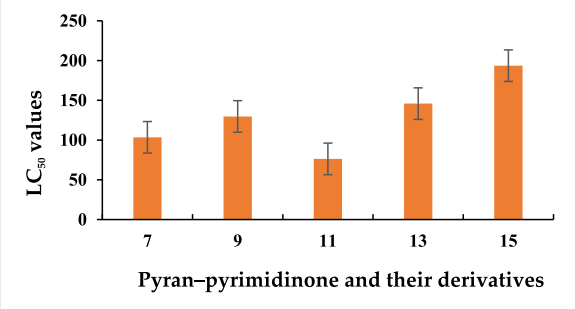

Fig. 3. Larvicidal activity of pyran–pyrimidinone hybrids against the 3rd larval instar of *Culex pipiens* after 48 h of exposure.

2.3.2. Effect on esterase enzyme activities

The effects of the synthesized compounds on esterase enzyme activities in *Cx. pipiens* larvae are summarized in Table 4. Significant reductions in AChE, α-esterase, and β-esterase activities were observed in treated larvae compared with the untreated control group ($P < 0.05$). Compound **11** exhibited the strongest inhibitory effect on AChE activity, reducing the enzyme activity to 5.17 nmol ACh hydrolyzed/min/mg protein, followed by compound **7**. Similarly, α- and β-esterase activities were markedly decreased in larvae treated with compounds **11** and **7**. In contrast, compound **15** showed relatively weak inhibitory effects, with enzyme activity values close to those of the control group. These findings show that the larvicidal activity of the tested compounds may partially involve disruption of the mosquito nervous system through esterase inhibition.

The biochemical tests showed that all tested compounds significantly inhibited acetylcholinesterase and α-esterase and β-esterase enzyme activity. AChE activity decreased from approximately 11.15±0.07 (control) to values as low as 5.17±0.24 nmol ACh hydrolyzed/min/mg protein, which showed a decrease of almost 50 percent in enzyme function, as evaluated in hybrid **11**.

2.3.3. Effect on digestive enzyme activities

The digestive enzymes of *Cx. pipiens* larvae experienced major changes after they received the synthesized compounds, as shown in Table 5. The treated larvae exhibited lower protease activities than the untreated control group, especially in the group that received compound **11** treatment. Most treated groups showed increased acid phosphatase activity when compared to the control group, while alkaline phosphatase activity showed a general decline after treatment. The strongest biochemical alterations occurred when larvae received exposure to compounds **11** and **7**, which caused major disruptions in their digestive metabolism and nutrient absorption.

Table 2
Efficacy of pyran–pyrimidinone hybrids on *Culex pipiens* larval mortality, 24 and 48 h post-treatment.

Time	Compounds	Concentration (μg/mL)					
		0	50	125	250	500	1000
24	7	0.00 ± 0.00^{aF}	15.00 ± 0.00^{aE}	36.67 ± 1.67^{bD}	76.67 ± 1.67^{bC}	96.67 ± 1.67^{bB}	100.0 ± 0.00^{aA}
	9	0.00 ± 0.00^{aF}	15.00 ± 0.00^{aE}	25.00 ± 2.89^{cD}	55.00 ± 2.89^{cC}	80.00 ± 2.89^{cB}	100.0 ± 0.00^{aA}
	11	0.00 ± 0.00^{aE}	15.00 ± 0.00^{aD}	48.33 ± 3.33^{aC}	88.33 ± 1.67^{aB}	100.0 ± 0.00^{aA}	100.0 ± 0.00^{aA}
	13	0.00 ± 0.00^{aF}	15.00 ± 0.00^{aE}	20.00 ± 0.00^{dD}	45.00 ± 2.89^{dC}	75.00 ± 0.00^{dB}	100.0 ± 0.00^{aA}
	15	0.00 ± 0.00^{aF}	15.00 ± 0.00^{aE}	16.67 ± 1.67^{eD}	43.33 ± 1.67^{eC}	65.00 ± 2.89^{eB}	96.67 ± 3.33^{bA}
	Temephos	85.00±0.00					
48	7	0.00 ± 0.00^{aE}	20.00 ± 0.00^{bD}	45.00 ± 5.00^{bC}	85.00 ± 2.89^{bB}	100.0 ± 0.00^{aA}	100 ± 0.00^{aA}
	9	0.00 ± 0.00^{aE}	16.67 ± 1.67^{cD}	33.33 ± 3.33^{cC}	73.33 ± 1.67^{cB}	100.0 ± 0.00^{aA}	100 ± 0.00^{aA}
	11	0.00 ± 0.00^{aE}	28.33 ± 3.33^{aD}	63.33 ± 3.33^{aC}	96.67 ± 3.33^{aB}	100.0 ± 0.00^{aA}	100 ± 0.00^{aA}
	13	0.00 ± 0.00^{aF}	15.00 ± 0.00^{cE}	26.67 ± 1.67^{dD}	70.00 ± 2.89^{dC}	95.00 ± 2.89^{bB}	100 ± 0.00^{aA}
	15	0.00 ± 0.00^{aF}	11.67 ± 1.67^{dE}	23.33 ± 1.67^{eD}	50.00 ± 2.89^{eC}	85.00 ± 2.89^{cB}	100 ± 0.00^{aA}
	Temephos	100±0.00					

a, b & c: There is no significant difference ($P > 0.05$) between any two means for each group compound within the same column that has the same superscript letter. A, B & C: There is no significant difference ($P > 0.05$) between any two means within the same row that have the same superscript letter. Temephos: 0.25 μg/mL.

Table 3
Lethal concentrations (μg/mL) of pyran–pyrimidinone hybrids on *Culex pipiens* mortality, 24 and 48 h post-treatment.

Time (h)	Cpd.	LC_{50} (Low-Up.)	LC_{90} (Low-Up.)	LC_{95} (Low-Up.)	Slope ± SE	X^2 (sign.)
24	**7**	128.36 (113.09–144.44)	382.07 (329.72–455.63)	520.51 (438.12–643.17)	2.705±0.179	0.801 (0.849)
	9	200.55 (170.59–235.31)	946.75 (727.54–1345.02)	1469.94 (1070.16–2261.07)	1.901±0.162	1.778 (0.619)
	11	103.19 (91.99–115.30)	248.92 (213.66–302.68)	319.49 (267.04–404.31)	3.351±0.275	3.351 (0.275)
	13	216.44 (102.91–432.67)	841.07 (752.88–4297.60)	1235.77 (1264.15–8625.68)	2.174±0.162	19.443 (0.000)
	15	252.81 (120.37–550.19)	1128.83 (1095.71–7770.84)	1725.19 (1940.75–17,381.24)	1.972±0.154	18.449 (0.000)
48	**7**	103.46 (91.25–116.49)	277.54 (236.17–340.82)	367.12 (303.40–470.96)	2.990±0.242	3.390 (0.335)
	9	129.69 (114.47–145.98)	373.44 (319.66–451.60)	503.99 (420.00–633.37)	2.790±0.196	6.065 (0.108)
	11	76.29 (66.75–85.83)	195.75 (170.80–231.38)	255.68 (217.78–313.73)	3.131±0.248	0.928 (0.818)
	13	145.84 (128.62–164.64)	427.00 (361.40–525.31)	579.01 (475.98–742.73)	2.747±0.200	6.699 (0.082)
	15	193.57 (120.25–300.40)	643.47 (489.43–1501.23)	904.51 (705.34–2447.00)	2.456±0.176	11.613 (0.008)

Table 4
The effect of pyran–pyrimidinone hybrids on the various esterase enzymes in mosquitoes.

Compounds	Acetylcholinesterase (nmol ACh hydrolyzed/ min/mg protein)	α-Esterase (α-EST) (mmol/ min/mg protein)	β-Esterase (β-EST) (mmol/ min/mg protein)
7	05.31 ± 0.06^{c}	1.06 ± 0.05^{b}	1.53 ± 0.09^{b}
9	07.38 ± 0.24^{d}	1.42 ± 0.03^{c}	1.84 ± 0.06^{c}
11	05.17 ± 0.24^{d}	1.04 ± 0.03^{c}	1.45 ± 0.06^{c}
13	09.02 ± 0.29^{b}	1.71 ± 0.33^{a}	2.76 ± 0.24^{ab}
15	11.93 ± 0.21^{e}	2.31 ± 0.09^{c}	03.54 ± 0.1^{c}
Control	11.15 ± 0.07^{a}	2.21 ± 0.05^{a}	3.48 ± 0.11^{a}

a, b & c: There is no significant difference ($P > 0.05$) between any two means, within the same column have the same superscript letter.

Table 5
The effect of pyran–pyrimidinone hybrids on the activities of digestive enzymes in mosquitoes.

Compounds	Acid protease (U/mg protein)	Alkaline protease (U/mg protein)	Acid phosphatase (U/mg protein)	Alkaline phosphatase (U/mg protein)
7	05.56 ± 0.03^{a}	07.25 ± 0.03^{a}	3.04 ± 0.03^{a}	0.53 ± 0.03^{a}
9	07.01 ± 0.02^{b}	08.89 ± 0.13^{b}	2.33 ± 0.02^{b}	0.69 ± 0.03^{a}
11	05.31 ± 0.01^{c}	07.16 ± 0.08^{c}	3.00 ± 0.01^{c}	0.48 ± 0.03^{a}
13	08.28 ± 0.09^{a}	10.49 ± 0.46^{a}	2.04 ± 0.23^{a}	0.89 ± 0.03^{a}
15	11.09 ± 0.16^{d}	14.32 ± 0.08^{d}	1.55 ± 0.06^{d}	1.16 ± 0.03^{a}
Control	12.37 ± 0.03^{a}	16.49 ± 0.15^{a}	1.27 ± 0.03^{a}	1.18 ± 0.46^{a}

a, b & c: There is no significant difference ($P > 0.05$) between any two means within the same column that have the same superscript letter.

The digestive enzyme functions experienced major alterations because the tested derivatives produced their effects. The acid protease activity showed a control value of 12.37±0.03 U/mg protein, which dropped to approximately 5.31±0.01 U/mg protein for treated hybrid larvae **11**. The observed reductions in protease and phosphatase activities may reflect impairment of nutrient digestion and metabolic processes in mosquito larvae. The physiological disturbances that occur in this process will cause negative effects on the growth and survival of larvae.

2.3.4. Effect on biological macromolecules

The effects of the synthesized pyran-pyrimidinone hybrids on the contents of biological macromolecules in *Cx. pipiens* larvae are shown in Table 6. The treated larvae showed significant decreases in protein, carbohydrate, and lipid contents when compared to the control group.

Table 6
The effect of pyran–pyrimidinone hybrids on contents of the biological macromolecules in mosquitoes.

Compounds	Protein content (mg/mL)3	Carbohydrate content (mg/mL)	Lipid content (mg/mL)
7	07.95 ± 0.05^{a}	2.71 ± 0.93^{a}	0.83 ± 0.07^{a}
9	10.36 ± 0.03^{c}	3.99 ± 0.50^{c}	1.17 ± 0.03^{b}
11	07.82 ± 0.03^{c}	2.53 ± 0.66^{c}	0.81 ± 0.19^{b}
13	12.96 ± 0.22^{b}	4.21 ± 0.82^{b}	1.27 ± 0.05^{b}
15	17.57 ± 0.02^{c}	5.91 ± 0.44^{d}	1.72 ± 0.06^{c}
Control	17.95 ± 0.05^{a}	6.03 ± 0.93^{a}	1.77 ± 0.07^{a}

a, b & c: There is no significant difference ($P > 0.05$) between any two means within the same column that have the same superscript letter.

The greatest protein and carbohydrate reduction occurred through compound **11**, while compound **7** provided the second highest in the reduction effect. The tested compounds led to decreased lipid levels in most treatment groups, which resulted in metabolic and energy reserve impairment for mosquito larvae.

2.3.5. Effect on oxidative stress and antioxidant biomarkers

The synthesized compounds induced significant changes in antioxidant enzyme activity and oxidative damage indicators of *Cx. pipiens* larvae after treatment with the synthesized compounds. A significant decrease was recorded in the activities of superoxide dismutase (SOD), glutathione S-transferase (GST), and catalase when exposed to these hybrids. Compound **11** was the most active inhibitor and reduced SOD activity significantly to 1.30±0.24 units/g tissue compared to 3.07 ±0.07 units/g tissue in the control group. Also, the activities of GST and CAT were decreased to 22.98±0.03 units/g tissue and 2.14±0.06 U/mg protein/min, respectively, from their initial control values of 54.06 ±0.05 units/g tissue and 4.34±0.11 U/mg protein/min. There was also a significant depletion of reduced glutathione levels to 0.95±0.09 μg/mg protein in larvae treated with hybrid **11** compared with 2.17 ±0.11 μg/mg protein in the untreated control.

This depletion of the antioxidant defense system was associated with a significant increase in markers of oxidative stress, where the results showed that compound **11** induced the highest levels of lipid peroxidation (LPO) and total protein carbonyl (TPC) content in the larvae (7.81±0.06 nmol/g tissue and 13.24±0.06 nmol/mg protein, respectively) compared to the control group (3.42±0.11 nmol/g tissue and 6.10±0.11 nmol/mg protein). On the other hand, compound **15** was comparatively lower in biochemical parameters, as the enzyme activities and oxidative markers were more similar to those observed in the untreated control. Compounds with the highest larvicidal potency exhibited the most significant suppression of antioxidant defenses and the greatest increase in markers of oxidative damage (Table 7).

The study found that synthesized compounds caused major biochemical changes in *Culex pipiens* larvae after researchers conducted oxidative stress tests. The antioxidant enzyme activities, which included SOD, GST, and CAT, experienced significant decreases that reached approximately 40 to 60 percent of their normal levels, while GSH levels

Table 7
The effect of pyran–pyrimidinone hybrids on the markers of the antioxidant defense in mosquitoes.

Compounds	SOD (units/g tissue)	GST (units/g tissue)	CAT (U/mg protein/min)	GSH (μg/mg protein)	LPO (nmol/g tissue)	TPC (nmol/mg protein)
7	1.32±0.06^{d}	23.97±0.05^{b}	2.01±0.09^{b}	1.27±0.06^{c}	7.75±0.09^{b}	13.00±0.09^{b}
9	1.50±0.24^{d}	24.02±0.03^{c}	2.12±0.06^{c}	1.08±0.06^{c}	7.68±0.06^{c}	11.86±0.06^{c}
11	1.30±0.24^{c}	22.98±0.03^{c}	2.14±0.06^{c}	0.95±0.09^{b}	7.81±0.06^{c}	13.24±0.06^{c}
13	2.30±0.29^{b}	41.53±0.33^{a}	3.40±0.24^{ab}	1.51±0.24^{ab}	4.35±0.24^{ab}	7.75±0.24^{ab}
15	2.97±0.21^{e}	51.75±0.09^{c}	4.30±0.10^{c}	2.12±0.10^{c}	3.34±0.10^{c}	6.13±0.10^{c}
Control	3.07±0.07^{a}	54.06±0.05^{a}	4.34±0.11^{a}	2.17±0.11^{a}	3.42±0.11^{a}	6.10±0.11^{a}

a, b & c: There is no significant difference ($P > 0.05$) between any two means within the same column that have the same superscript letter.

showed corresponding drops in concentration. The study found that oxidative damage markers, which included LPO, increased from 3.42 ±0.11 nmol/g tissue (control) to approximately 7–8 nmol/g tissue (≈2-fold increase), while TPC showed a similar pattern of increase. The tested compounds produce excessive amounts of ROS, which results in oxidative damage to cellular components.

The tested compounds showed the strongest larvicidal and biochemical effects through **11**, which established a direct link between larval death and the two processes of enzymatic inhibition and oxidative stress induction. The derivative shows increased activity because its chemical structure enables it to disrupt vital life functions that mosquitoes require for their development.

2.3.6. Antioxidant activity

The antioxidant activity of ascorbic acid (employed as a reference standard) and five synthesized organic compounds (**7, 9, 11, 13**, and **15**) was evaluated using the DPPH free radical scavenging assay as an in vitro model for assessing radical quenching capacity (Table 8). Utilizing a four-parameter logistic (4PL) sigmoidal framework, nonlinear regression analysis was used to determine the IC_{50} values, which provides a robust and accurate description of concentration–response relationships and is widely accepted for biological and chemical activity profiling. The calculated IC_{50} values demonstrated clear differences in antioxidant potency among the tested synthetic compounds. 3.98 μg/mL is the lowest IC_{50} value ascorbic acid demonstrated the highest radical scavenging activity, confirming its role as a highly efficient hydrogen and electron donor. Among the synthesized compounds, **11** demonstrated the potent antioxidant activity with an IC_{50} measurement of 4.30 μg/mL, followed by **7** (4.85 μg/mL), **9** (5.42 μg/mL), **13** (6.05 μg/mL), and **15** (6.73 μg/mL), which displayed the weakest activity among the tested derivatives (Fig. 4).

These results indicate that structural variations within the synthesized series significantly influence radical scavenging efficiency, likely due to differences in electronic distribution, substituent effects, and the ability to stabilize the resulting radical species after hydrogen or electron donation. Compounds containing more electron-donating or resonance-stabilizing groups appear to exhibit enhanced antioxidant activity, as reflected by their lower IC_{50} values [39,40]. Overall, all synthesized compounds demonstrated measurable antioxidant activity, although they were less potent than the reference standard ascorbic acid. The observed structure–activity relationship suggests that subtle modifications in molecular architecture can markedly affect the redox behavior of these compounds [41,42].

Table 8
DPPH assay.

Conc.	Ascorbic Acid	7	9	11	13	15
1000	98	97.3	97	97.6	96.7	96.3
500	96	95.1	94.5	95.4	94	93.4
250	92.8	91.6	90.9	92.1	90.3	89.4
125	86.4	85	84.1	85.9	83.1	82.1
62.5	81	79	77.7	79.8	76.6	75.3
31.25	73.2	71	69.6	72	68.3	67
15.625	65.8	63.1	61.7	64.4	60.4	59.1
7.8125	58	55.1	53.6	56.5	52.1	50.7
3.9	50.3	48.3	46.9	49.7	45.6	44.3
1.95	42.8	40.2	39	42.1	37.7	36.5

2.4. Computational studies

2.4.1. Fukui function and dual descriptor

Fukui function analysis was performed to determine which atomic sites are the most reactive in compounds **7, 9, 11, 13**, and **15** using the optimized structures (Fig. 5) of these compounds. The condensed Fukui indices (f_k^+), (f_k^-) and (f_k^0) were used to predict the preferred centers for nucleophilic, electrophilic, and radical attack, respectively, while the dual descriptor $\Delta f(r) = [f^+(r) - f^-(r)]$ was used to distinguish the local electrophilic and nucleophilic characters. Negative values indicate sites more susceptible to electrophilic attacks, whereas positive $\Delta f(r)$ values indicate sites more favorable for nucleophilic attacks.

Fukui functions (Tables 8–10 and S6-S7) derived from NBO atomic charges are calculated according to the following equations [43]:

$$\text{Electrophilicattack}: f_k^- = q_k(N_0) - q_k(N_0 - 1)$$

$$\text{Nucleophilicattack}: f_k^+ = q_k(N_0 + 1) - q_k(N_0)$$

$$\text{Radicalattack}: f_k^0 = \tfrac{1}{2}(f_k^+ + f_k^-)$$

where the electronic population of atom k in a molecule in its neutral state anionic, and cationic states, respectively, is represented by qk, (N_0), (N_0 + 1), and (N_0 - 1).

The Fukui results indicate that nucleophilic attack is mainly directed toward polarized carbon atoms within the pyran ring and the attached substituent fragments, while electrophilic attack is favored at heteroatom-rich regions, in particular oxygen and nitrogen atoms. The common pyran-pyrimidinedione framework of the five compounds (Tables 9–11 and S6-S7) shows comparable reactivity behavior, with some differences caused by the attached substituents. In compound **7**, the most electrophilic attack favorable centers are N29, O31, O25, N36, O7, N9, O11, O8, and N3, which show negative $\Delta f(r)$ values (Table 9). These results indicate that the *O* and *N* atoms act as electron-rich centers. The highest f_k^+ values are mainly observed at C27, C35, C30, C12, C4, and C24, with positive $\Delta f(r)$ measurements, indicating that these atoms are the most probable sites for nucleophilic attack.

For compound **9**, the most negative $\Delta f(r)$ values are found at N32, N30, O29, O27, N23, O7, N9, and N3, suggesting that these heteroatoms are the preferred sites for electrophilic attack. In contrast, the largest nucleophilic attack sites are located mainly at C12, C13, C25, C26, C2, and C6, based on their high positive $\Delta f(r)$and f_k^+ values (Table 10). Compound **11** shows a similar pattern, where N1, N32, N24, O7, N28, N9, and C16 are the main electrophilic attack centers, while C25, C26, C12, C6, C2, C4, and C15 are the main nucleophilic attack centers (Table S6). The contribution of the carbamothioyl fragment in compound **11** appears to enhance the localization of reactive centers around the substituent-bearing region.

Compound **13** shows the most dual descriptor values are observed at N30, N10, N26, N16, N28, O11, N1, and N3, while strong nucleophilic susceptibility is at C25, C6, C17, C12, C2, and C15 (Table 11). This reflects the contribution of the hydrazonamide nitrogen atoms to the electron-rich regions of the molecule. In compound **15**, N1, N3, O11, N23, O7, O8, and Cl22 are more favorable for electrophilic attack,

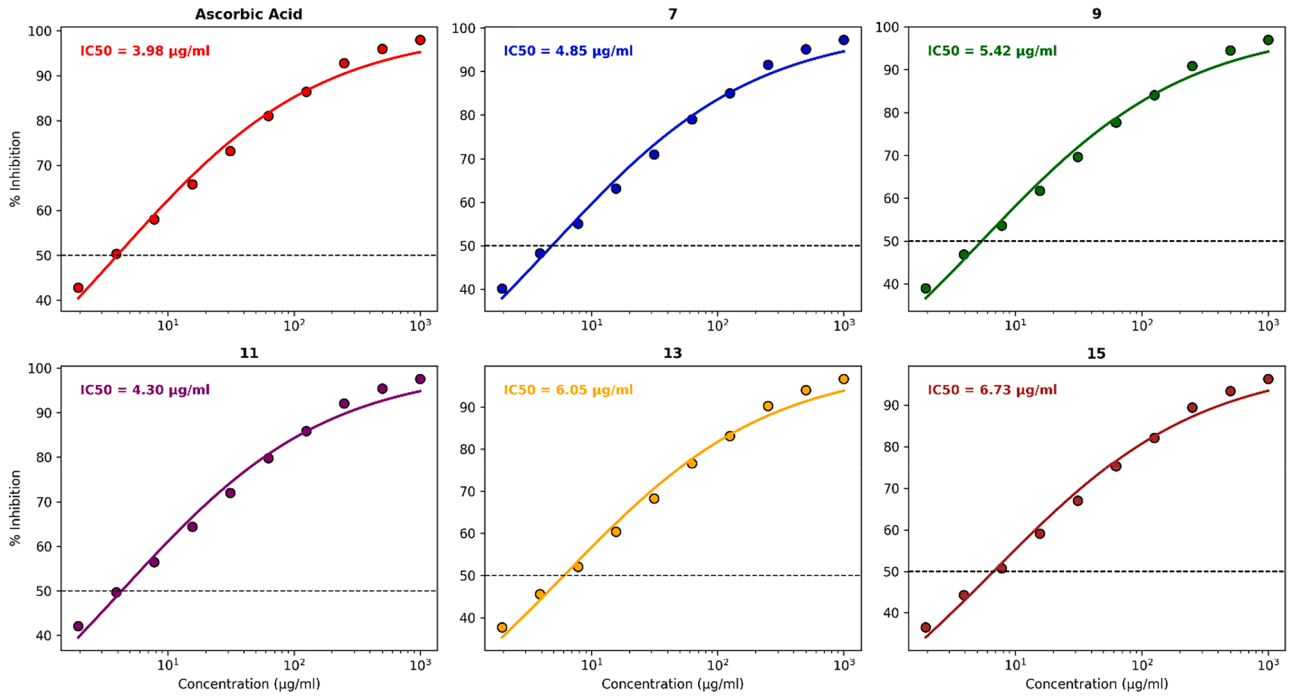

Fig. 4. Comparative antioxidant activity and IC_{50} determination of ascorbic acid and compounds using the DPPH radical scavenging assay.

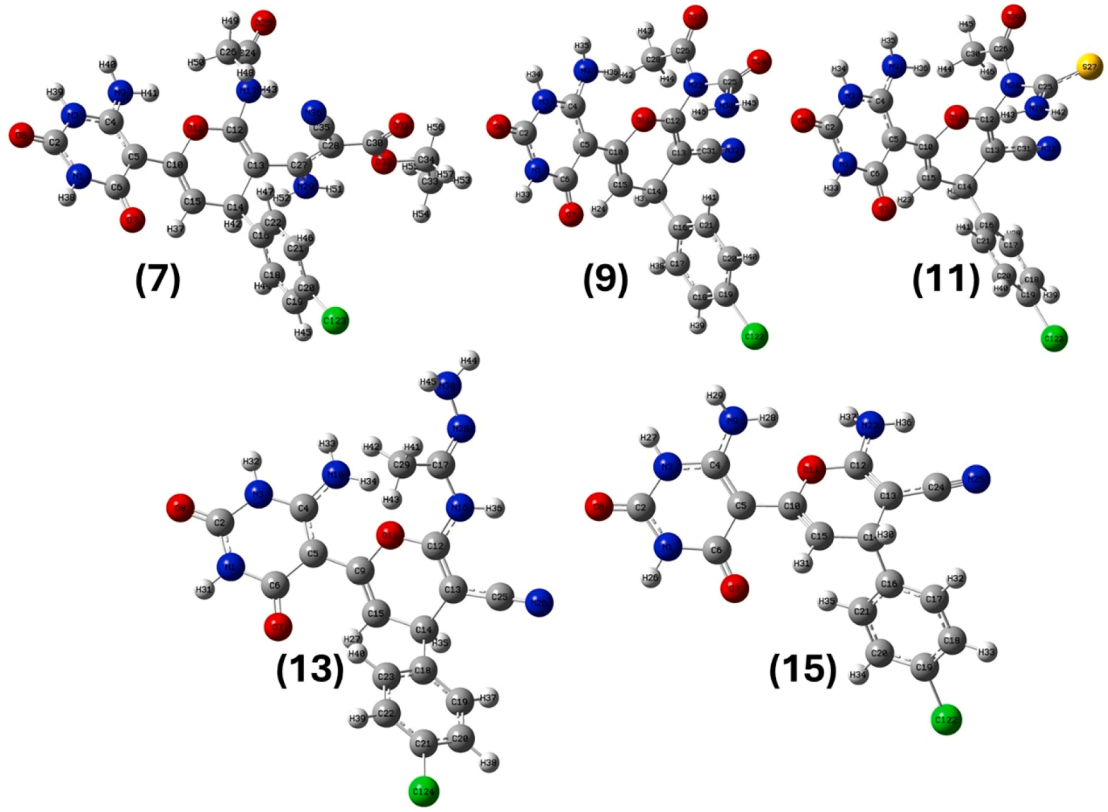

Fig. 5. The optimized molecular geometry of compounds **7, 9, 11, 13**, and **15** using DFT.

whereas the preferred nucleophilic attack sites are C6, C2, C24, C12, C19, C13, and C10. The high f_k^0 value of N25 in compound **15** also suggests that the amino nitrogen may contribute to radical-type interactions (Table S7).

2.4.2. Map of the molecular electrostatic potential (MEP)

The MEP maps of compounds **7, 9, 11, 13**, and **15** were analyzed to visualize the distribution of electron-rich and electron-deficient regions over the molecular surfaces. MEP analysis is widely used to predict the sites involved in the electrophilic and nucleophilic attack based on the

Table 9
Fukui analysis of compound **7**.

Compound 7									
Atom	f_k^-	f_k^+	f_k^0	$\Delta f(r)$	**Atom**	f_k^-	f_k^+	f_k^0	$\Delta f(r)$
N1	0.0067	0.0055	0.0061	-0.0012	**C30**	0.0033	0.0860	0.0446	0.0827
C2	-0.0016	0.0099	0.0042	0.0115	**O31**	0.0791	0.0227	0.0509	-0.0564
N3	0.0225	0.0019	0.0122	-0.0205	**O32**	0.0055	0.0083	0.0069	0.0028
C4	0.0273	0.0660	0.0467	0.0387	**C33**	-0.0039	-0.0061	-0.0050	-0.0022
C5	-0.0125	0.01,016	-0.00,116	0.02,264	**C34**	-0.0023	-0.0033	-0.0028	-0.0009
C6	-0.00,365	0.00,397	0.00,016	0.00,762	**C35**	0.00,366	0.08,978	0.04,672	0.08,612
O7	0.04,183	0.01,368	0.0278	-0.02,815	**N36**	0.06,461	0.02,648	0.0455	-0.0381
O8	0.06,043	0.03,948	0.0499	-0.02,095	**H37**	0.01,796	0.02,014	0.01,905	0.00,218
N9	0.04,284	0.01,699	0.0299	-0.02,585	**H38**	0.01,829	0.01,377	0.01,603	-0.0045
C10	0.02,881	0.02,715	0.02,798	-0.00,166	**H39**	0.01,885	0.01,303	0.01,594	-0.0058
O11	0.03,088	0.00,836	0.01,962	-0.02,252	**H40**	0.02,255	0.01,635	0.01,945	-0.0062
C12	0.00,152	0.08,171	0.0416	0.08,019	**H41**	0.0049	-0.0029	0.00,101	-0.0078
C13	-0.00,465	0.01,374	0.0045	0.01,839	**H42**	0.01,367	0.03,267	0.02,317	0.019
C14	-0.02,276	-0.00,523	-0.0140	0.01,753	**H43**	0.01,035	0.01,293	0.01,164	0.00,258
C15	0.01,953	0.0508	0.03,516	0.03,127	**H44**	0.01,139	0.00,919	0.01,029	-0.0022
C16	-0.00,223	-0.02,299	-0.01,261	-0.02,076	**H45**	0.01,784	0.01,646	0.01,715	-0.0014
N17	0.00,706	-0.00,808	-0.00,051	-0.01,514	**H46**	0.0147	0.01,274	0.01,372	-0.0019
C18	0.00,524	0.0204	0.01,282	0.01,516	**H47**	-0.0005	-0.0036	-0.0021	-0.0031
C19	0.02,215	0.01,047	0.01,631	-0.01,168	**H48**	-0.0010	0.00,113	0.0001	0.00,208
C20	0.02,089	0.01,455	0.01,772	-0.00,634	**H49**	0.01,866	0.02,104	0.01,985	0.00,238
C21	0.00,701	0.02,107	0.01,404	0.01,406	**H50**	-0.0083	0.0065	-0.0009	0.01,487
C22	0.00,184	-0.01,214	-0.00,515	-0.01,398	**H51**	0.01,254	0.01,898	0.01,576	0.00,644
C123	0.03,915	0.03,887	0.03,901	-0.00,028	**H52**	0.00,497	0.01,896	0.0120	0.01,399
C24	-0.00,631	0.05,633	0.02,501	0.06,264	**H53**	0.01,283	0.01,798	0.0154	0.00,515
O25	0.06,962	0.02,005	0.0448	-0.04,957	**H54**	0.00,144	0.00,391	0.0027	0.00,247
C26	-0.00,093	-0.00,456	-0.0027	-0.00,363	**H55**	0.0031	0.0047	0.0039	0.0016
C27	-0.01,627	0.09,496	0.0393	0.11,123	**H56**	0.00,756	0.01,069	0.0091	0.00,313
C28	-0.0314	0.04,071	0.0047	0.07,211	**H57**	0.00,619	0.01,034	0.0083	0.00,415
N29	0.02,219	-0.05,557	-0.01,669	-0.07,776					

Table 10
Fukui analysis of compound **9**.

Compound 9									
Atom	f_k^-	f_k^+	f_k^0	$\Delta f(r)$	**Atom**	f_k^-	f_k^+	f_k^0	$\Delta f(r)$
N1	0.00,823	0.00,688	0.00,755	-0.0013	**H24**	0.01,608	0.02,414	0.02,011	0.00,806
C2	-0.0321	0.04,278	0.00,532	0.07,491	**C25**	-0.0048	0.06,726	0.03,120	0.07,211
N3	0.02,781	0.00,262	0.01,521	-0.0252	**C26**	-0.0068	0.05,858	0.02,585	0.06,545
C4	0.03,066	0.06,105	0.04,585	0.03,039	**O27**	0.07,708	-0.0067	0.03,517	-0.0838
C5	0.01,728	0.02,749	0.02,238	0.01,021	**C28**	-0.0005	-0.0050	-0.0028	-0.0045
C6	-0.0059	0.05,519	0.02,462	0.06,114	**O29**	0.0784	-0.0115	0.03,346	-0.0898
O7	0.05,151	0.01,678	0.03,414	-0.0347	**N30**	0.06,691	-0.0517	0.00,759	-0.1186
O8	0.07,069	0.04,749	0.05,909	-0.0232	**C31**	-0.0214	0.01,024	-0.0056	0.03,159
N9	0.05,564	0.02,164	0.03,864	-0.0340	**N32**	0.26,233	-0.0655	0.09,844	-0.3278
C10	0.02,868	0.04,846	0.03,857	0.01,978	**H33**	0.02,067	0.01,659	0.01,863	-0.0041
O11	0.01,792	0.01,081	0.01,436	-0.0071	**H34**	0.02,182	0.01,591	0.01,886	-0.0059
C12	-0.0036	0.13,108	0.0637	0.13,476	**H35**	0.02,534	0.02,034	0.02,284	-0.0050
C13	0.01,995	0.09,637	0.05,816	0.07,642	**H36**	0.01,053	-0.0015	0.00,449	-0.0120
C14	-0.0212	-0.0154	-0.0183	0.00,576	**H37**	0.03,221	0.02,073	0.02,647	-0.0115
C15	0.0411	0.04,729	0.04,419	0.00,619	**H38**	0.01,612	0.01,333	0.01,472	-0.0028
C16	0.02,506	-0.0173	0.00,387	-0.0424	**H39**	0.02,081	0.01,992	0.02,036	-0.0009
C17	0.00,901	0.03,386	0.02,143	0.02,485	**H40**	0.0189	0.01,741	0.01,815	-0.0015
C18	0.02,741	0.00,877	0.01,809	-0.0186	**H41**	0.00,807	-0.0017	0.00,318	-0.0097
C19	0.03,464	0.02,895	0.03,179	-0.0057	**H42**	-0.0119	-0.0049	-0.0084	0.00,702
C20	0.01,107	0.02,819	0.01,963	0.01,712	**H43**	0.01,504	0.0247	0.01,987	0.00,966
C21	0.01,079	-0.0106	0.00,011	-0.0214	**H44**	0.00,333	-0.001	0.00,116	-0.0043
C122	0.06,434	0.04,938	0.05,686	-0.0149	**H45**	0.0116	0.01,876	0.01,518	0.00,716
N23	0.06,618	-0.0176	0.02,427	-0.0838	**H46**	-0.0097	-0.0025	-0.0061	0.00,722

color scale. Negative electrostatic potential is represented by the red parts, positive potential by the blue regions, and almost neutral regions by the green parts.

The electrostatic potential values were distributed within the ranges -8.873×10^{-2} to $+8.873 \times 10^{-2}$ for compound **7**, -9.643×10^{-2} to $+9.643 \times 10^{-2}$ for compound **9**, -1.000×10^{-1} to $+1.000 \times 10^{-1}$ for compound **11**, -9.895×10^{-2} to $+9.895 \times 10^{-2}$ for compound **13**, and -8.797×10^{-2} to $+8.797 \times 10^{-2}$ for compound **15** as shown in Fig. 6. These values indicate compounds **11** and **13** display the highest electrostatic contrast, suggesting more pronounced charge separation across their molecular surfaces, while compound **15** shows the lowest overall potential range among the studied derivatives. The graphical representation of the electrostatic potential shows the regions with negative potential are localized mainly around the carbonyl and oxygen atoms of the pyrimidinedione moiety and the heteroatom-containing substituents. This indicates that these regions have electron-rich character, making them possible hydrogen bond acceptors. In contrast, the positive potential regions are mostly observed around the amino and NH

Table 11
Fukui analysis of compound **13**.

Compound 13									
Atom	f_k^-	f_k^+	f_k^0	$\Delta f(r)$	**Atom**	f_k^-	f_k^+	f_k^0	$\Delta f(r)$
N1	0.0358	-0.0172	0.00,927	-0.0530	**Cl24**	0.04,655	0.0404	0.04,347	-0.0062
C2	-0.0013	0.05,153	0.02,514	0.05,278	**C25**	-0.0693	0.04,665	-0.0113	0.11,591
N3	0.0225	-0.0095	0.00,652	-0.0319	**N26**	0.05,988	0.00,329	0.03,158	-0.0565
C4	0.04,257	0.0585	0.05,053	0.01,593	**H27**	0.02,143	0.02,196	0.02,169	0.00,053
C5	0.01,655	0.02,254	0.01,954	0.00,599	**N28**	0.04,848	-0.0466	0.00,091	-0.0951
C6	-0.0302	0.03,721	0.00,347	0.06,747	**C29**	-0.0103	-0.0069	-0.0085	0.00,339
O7	0.05,452	0.03,095	0.04,273	-0.0235	**N30**	0.06,515	0.02,156	0.04,335	-0.0435
O8	0.06,825	0.05,807	0.06,316	-0.0101	**H31**	0.01,529	0.01,998	0.01,763	0.00,469
C9	0.01,277	0.03,242	0.02,259	0.01,965	**H32**	0.01,381	0.0186	0.01,620	0.00,479
N10	0.06,026	0.03,131	0.04,578	-0.0289	**H33**	0.01,586	0.02,236	0.01,911	0.0065
O11	0.03,634	0.00,081	0.01,857	-0.0355	**H34**	-0.0058	0.00,328	-0.0013	0.0091
C12	0.00,261	0.06,449	0.03,355	0.06,188	**H35**	0.0463	0.02,095	0.03,362	-0.0253
C13	0.01,196	0.01,549	0.01,372	0.00,353	**H36**	0.01,684	0.02,105	0.01,894	0.00,421
C14	-0.0226	-0.0131	-0.0178	0.00,955	**H37**	0.00,405	0.00,755	0.0058	0.0035
C15	-0.0094	0.02,654	0.00,854	0.03,599	**H38**	0.01,485	0.01,677	0.01,581	0.00,192
N16	0.05,117	0.00,339	0.02,728	-0.0477	**H39**	0.01,351	0.01,459	0.01,405	0.00,108
C17	-0.0222	0.04,416	0.01,097	0.06,638	**H40**	-0.0037	-0.0039	-0.0038	-0.0002
C18	-0.0237	-0.0082	-0.0159	0.01,552	**H41**	0.02,539	0.02,135	0.02,337	-0.0040
C19	0.00,093	0.01,323	0.00,708	0.0123	**H42**	0.01,394	0.0103	0.01,212	-0.0036
C20	0.01,412	0.01,124	0.01,268	-0.0029	**H43**	0.00,724	-0.0011	0.00,307	-0.0083
C21	0.01,159	0.02,394	0.01,776	0.01,235	**H44**	0.0249	0.01,797	0.02,143	-0.0069
C22	0.01,047	0.01,852	0.01,449	0.00,805	**H45**	0.02,104	0.01,474	0.01,789	-0.0063
C23	0.00,074	-0.0031	-0.0012	-0.0038					

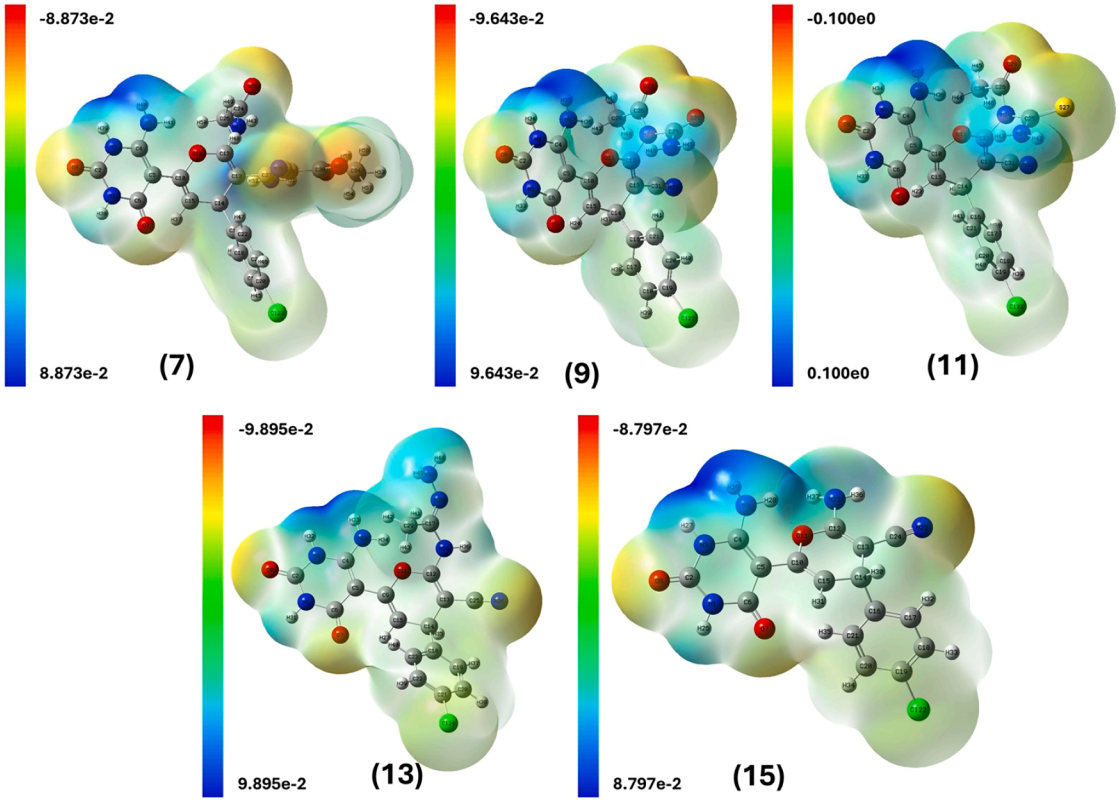

Fig. 6. The optimized compounds **7, 9, 11, 13**, and **15**′s MEP map.

hydrogen atoms, especially those attached to the pyrimidinone and amino-functionalized fragments. These blue areas correspond to electron-deficient sites and may act as hydrogen bond donors or centers susceptible to nucleophilic interaction. The phenyl and pyran regions are mostly covered by green to pale yellow surfaces, indicating comparatively neutral electrostatic character. Overall, the MEP results suggest that the biological or intermolecular recognition behavior of these compounds is mainly governed by the oxygen, nitrogen, and sulfur-containing functional groups, which provide the principal sites for electrostatic and hydrogen bonding interactions. Therefore, the biological activity of these compounds can be attributed to the differences in the distribution of electrostatic potential.

2.4.3. Frontier molecular orbital (FMO) analysis

FMO was performed to evaluate the electronic behavior, stability, and possible charge transfer characteristics of compounds **7, 9, 11, 13**,

and **15**. The energy difference between HOMO and LUMO provides useful information about molecular stability and chemical reactivity. A molecule with a significant energy gap is hard and stable, whereas a molecule with a tiny gap is soft and consequently more reactive [44].

The energy gaps between HOMO and LUMO were obtained at 4.247, 4.340, 4.040, 4.444, and 4.819 eV for compounds **7, 9, 11, 13**, and **15**, respectively, as shown in Fig. 7 and Table 12. Compound **15** exhibited the largest energy gap, indicating the highest electronic stability and the lowest tendency toward intramolecular charge transfer. On the other hand, compound **11** showed the smallest gap, suggesting relatively higher electronic softness and greater ability to participate in charge transfer interactions, while **7, 9**, and **13** showed intermediate gaps, indicating a moderate degree of electronic stability.

As presented in Fig. 7, the HOMO is mainly localized over the conjugated heterocyclic framework in the synthesized compounds, suggesting that these areas are the main locations that donate electrons. The LUMO is more extended toward the electron-withdrawing parts of the molecules, indicating an intramolecular donor-acceptor character, where electron density can be transferred from the π- rich heteroaromatic regions toward the more electron-deficient functional groups.

Using the following formulas, the global reactivity descriptors of compounds **7, 9, 11, 13**, and **15** are calculated from the HOMO and LUMO energies (Table 12) [45]:

$$\text{Hardness}: \eta = \frac{IP-Ea}{2}$$

$$\text{Chemicalpotential}: \mu = -\frac{(IP+Ea)}{2}$$

$$\text{Softness}: S = \frac{1}{\eta}$$

$$\text{Electronegativity}: \chi = \frac{IP+Ea}{2}$$

The obtained results showed that the electron affinity values followed the order **11**>**9** > **7** > **13**>**15**, suggesting that compound **11** has the strongest electron-accepting tendency among the series. This may be related to the presence of the carbamothioyl group, which contributes to stabilization of the LUMO level. The chemical hardness values increased in the order **11**<**7** < **9** < **13**<**15**, confirming that compound **11** is the softest and the most polarized derivative, whereas compound **15** is the hardest and the least reactive toward charge transfer. This trend is also supported by the softness values, where compound **11** showed the highest softness value (0.495 eV^{-1}) and compound **15** the lowest (0.415 eV^{-1}). The chemical potential values were negative for all compounds, indicating their overall electronic stability. Compound **9** showed the most negative chemical potential and the highest electronegativity value (4.059 eV), suggesting a stronger tendency to attract electron density. These findings are consistent with orbital distribution patterns and support the role of heteroatoms in controlling the electronic characteristics of these pyran pyrimidinedione derivatives.

Table 12
HOMO (eV), LUMO (eV), ionization potential (eV), electron affinity (eV), chemical potential (eV), chemical hardness (eV), softness (eV^{-1}), and electronegativity (eV) values of hybrids **7, 9, 11, 13**, and **15** in eV calculated using HOMO/LUMO energies.

Reactivity parameters	7	9	11	13	15
HOMO (eV)	-5.948	-6.229	-5.985	-5.714	-5.976
LUMO (eV)	-1.701	-1.889	-1.945	-1.270	-1.157
Ionization potential (IP)	5.948	6.229	5.985	5.714	5.976
Electron affinity (Ea)	1.701	1.889	1.945	1.270	1.157
Chemical potential (μ)	-3.825	-4.059	-3.965	-3.492	-3.566
Chemical hardness (η)	2.124	2.170	2.020	2.222	2.410
Softness (S)	0.471	0.461	0.495	0.450	0.415
Electronegativity (χ)	3.825	4.059	3.965	3.492	3.566

The calculated HOMO-LUMO energy gaps of hybrids **7, 9, 11, 13**, and **15** fall in the range of 4.040 to 4.819 eV, indicating moderate electronic stability with variable charge-transfer ability. These values are consistent with previously reported DFT studies on structurally related pyran and chromene-carbonitrile derivatives. For example, Al Jahdaly reported a HOMO-LUMO gap of 4.949 eV for 2-amino-4-(4-hydroxy-3-methoxyphenyl)-7-methyl-4*H*-chromene-3-carbonitrile, using a B3LYP/6–311++G(d,p) based calculations [46]. Similar trends have been observed for dihydropyranopyran derivatives, where the reported HOMO-LUMO gaps ranged from 3.744 to 4.293 eV, and the compounds with larger gaps were considered more stable [47].

To better connect the computational findings with the experimental activity, computational findings were compared with the biophysical results of the synthesized derivatives. The 48 h larvicidal activity followed the order **11 > 7 > 9 > 13 > 15**, based on the LC_{50} values. Interestingly, this trend agrees well with the HOMO-LUMO energy gap and softness values. Compound **11**, which exhibited the strongest larvicidal effect, had the smallest HOMO-LUMO gap (4.040 eV) and the highest softness (0.495 eV^{-1}), suggesting greater electronic flexibility, easier charge redistribution, and higher interaction potential. In contrast, compound **15**, the least active derivative, showed the largest energy gap (4.819 eV) and the lowest softness (0.415 eV^{-1}), indicating higher electronic stability and lower tendency toward charge-transfer interactions.

The local reactivity descriptors further support this interpretation. Fukui, MEP, and Mulliken analyses showed that the most reactive regions are mainly associated with heteroatom-rich fragments, especially carbonyl, amino, cyano, and carbamothioyl/hydrazonamide groups. The structure-activity relationship (SAR) study of these derivatives

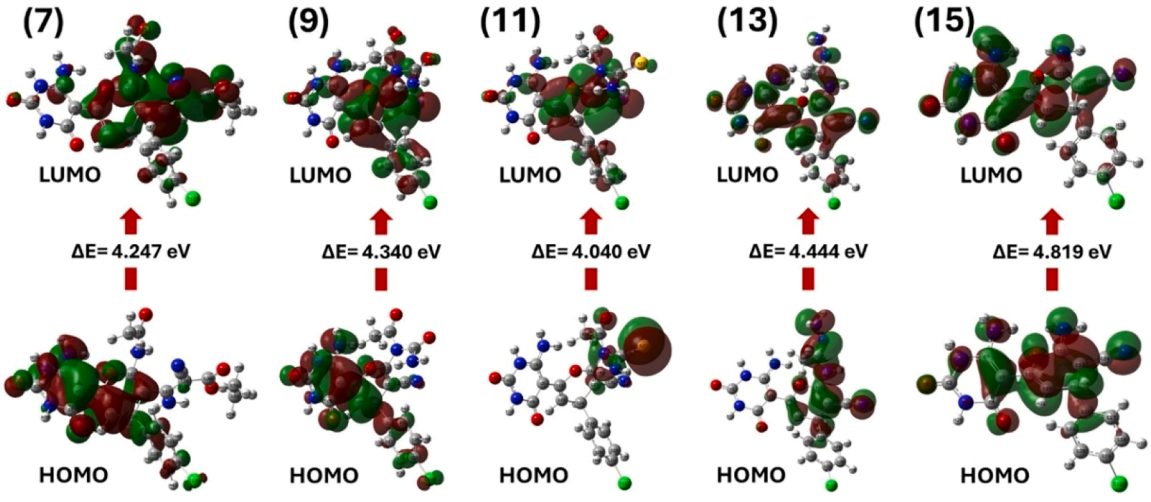

Fig. 7. Frontier molecular orbital (HOMO-LUMO) plots for the optimized hybrids **7, 9, 11, 13**, and **15**.

revealed that the superior activity of compound **11** may also be related to the presence of the carbamothioyl group, which introduces sulfur and additional heteroatom-based polarization into the molecule. This structural feature may enhance electrostatic and hydrogen bonding interactions with biological targets and facilitate disruption of enzymatic and oxidative stress pathways in larvae. This is consistent with the biochemical results, where compound **11** produced the strongest inhibition of AChE and esterases and caused pronounced oxidative stress effects. In contrast, compound **15** lacks the additional carbamothioyl substituent and showed weaker larvicidal and biochemical effects, in agreement with its higher hardness and lower softness.

2.4.4. Mulliken population analysis

It was purposed to examine the atomic charge distribution in the optimized structures of compounds **7, 9, 11, 13**, and **15**. This analysis provides a useful qualitative description of molecular polarization and helps identify electron-rich and electron-deficient centers within the molecular framework. Since Mulliken charges may be affected by the basis set, the discussion focuses mainly on general charge trends rather than absolute values [48].

The most negative Mulliken charges are mainly located on the heteroatoms, particularly the nitrogen and oxygen atoms, as shown in Fig. 8 and Table 13. In compounds **7, 9, 11**, and **15**, N1, N3, and N9 show high negative charges, while compound **13** shows the highest negative charge at N10. The oxygen atoms O7, O8, and O11 also display strong negative polarization in all the compounds. These sites represent electron-rich regions and may act as preferred centers for electrophilic attack and HBA interactions, in agreement with the MEP results.

On the other hand, several carbon atoms directly attached to electronegative atoms show positive charges, particularly C2, C4, and C6 in all compounds. This confirms their electron-deficient nature and possible susceptibility toward nucleophilic attack. Compound **13** shows the highest positive charge at C4, indicating stronger local polarization in this region.

The substituent affects the charge profile. Compound **11** contains a negatively charged sulfur atom, S27, which may contribute to its higher softness and smaller HOMO-LUMO gap. Compound **13** contains additional electron-rich nitrogen atoms from the hydrazonamide group, while compound **7** shows extra negative centers within the ethyl cyanoacrylate fragment.

The Mulliken charge distribution supports the MEP and FMO findings and confirms that the electronic behavior of these compounds is mainly controlled by the heteroatom-rich pyrimidinedione, amino, carbonyl, cyano, carbamothioyl, and hydrazonamide groups.

All larvicidal efficacy assessments were conducted under laboratory conditions, ensuring reproducibility and mechanism clarity. Future field validation studies remain essential to confirm efficacy under natural environmental variables. The current study did not assess toxicity to non-target aquatic organisms or the compound's persistence in the environment, as these assessments fall outside the scope of primary chemical and biochemical investigation. Similarly, although the multi-target mechanism is strongly supported by significant enzyme inhibition patterns and oxidative stress biomarkers, direct target validation represents a logical next step and is not a shortcoming of the current work. Within these clearly defined limitations, Compound **11** undoubtedly emerges as a highly promising leading candidate for further refinement and preclinical development, with in vitro efficacy serving as the foundation upon which future field and environmental studies should be built. It should be noted that the DFT descriptors used in this study do not establish the biological mechanism of action by themselves.

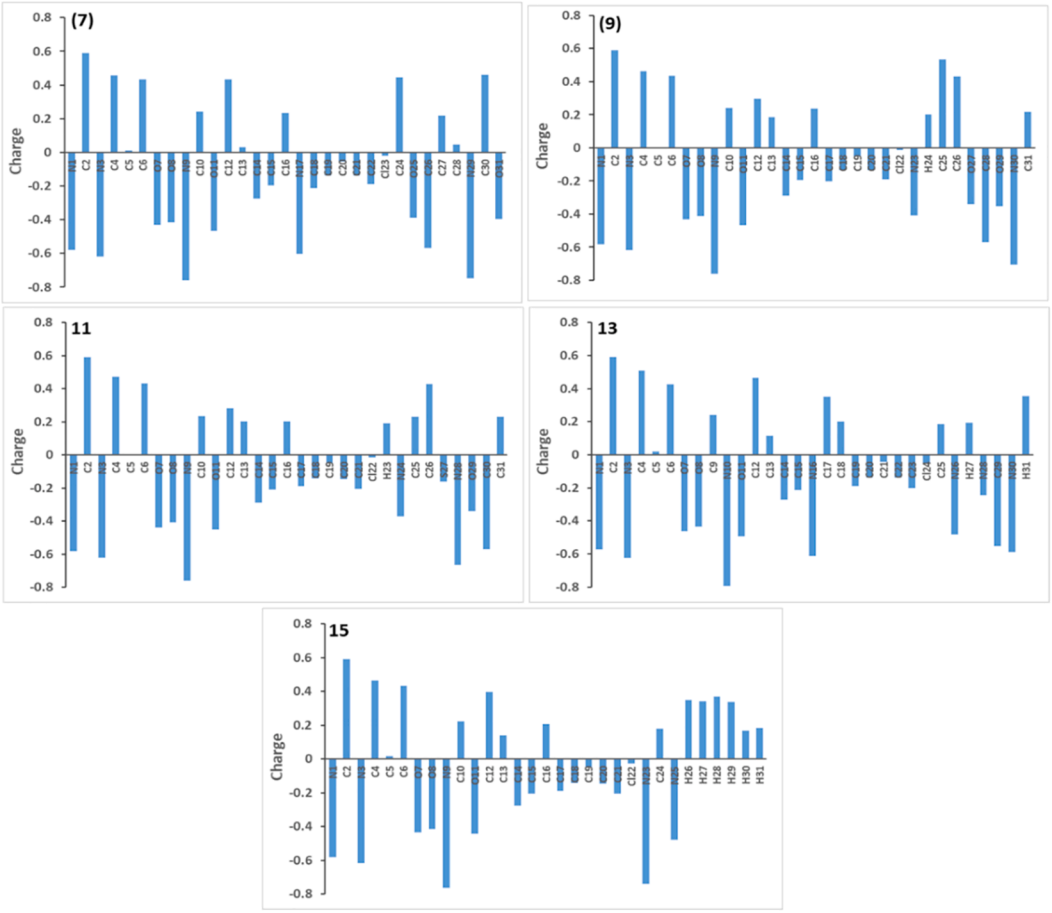

Fig. 8. Mulliken charge plots for the optimized hybrids **7, 9, 11, 13**, and **15**.

Table 13
Mulliken charges for compounds **7, 9, 11, 13**, and **15**.

7		9		11		13		15	
Atom	**Charge**	**Atom**	Charge	**Atom**	**Charge**	**Atom**	**Charge**	**Atom**	**Charge**
N1	-0.58,144	N1	-0.58,198	N1	-0.58,141	N1	-0.57,395	N1	-0.58,072
C2	0.589,061	C2	0.589,631	C2	0.592,317	C2	0.592,546	C2	0.589,477
N3	-0.61,871	N3	-0.62,001	N3	-0.62,137	N3	-0.62,515	N3	-0.6151
C4	0.458,324	C4	0.460,843	C4	0.469,891	C4	0.507,224	C4	0.464,501
C5	0.01,183	C5	0.004,326	C5	-0.00,038	C5	0.01,868	C5	0.014,902
C6	0.431,629	C6	0.433,272	C6	0.433,494	C6	0.424,928	C6	0.430,118
O7	-0.43,246	O7	-0.43,269	O7	-0.43,735	O7	-0.46,137	O7	-0.43,566
O8	-0.41,554	O8	-0.41,151	O8	-0.40,835	O8	-0.43,527	O8	-0.41,462
N9	-0.75,958	N9	-0.76,239	N9	-0.75,953	C9	0.239,347	N9	-0.76,518
C10	0.240,075	C10	0.239,341	C10	0.233,091	N10	-0.7924	C10	0.220,723
O11	-0.46,479	O11	-0.46,582	O11	-0.45,187	O11	-0.49,329	O11	-0.44,259
C12	0.432,484	C12	0.294,544	C12	0.281,062	C12	0.463,765	C12	0.397,321
C13	0.029,223	C13	0.184,036	C13	0.201,768	C13	0.114,379	C13	0.13,726
C14	-0.27,323	C14	-0.28,986	C14	-0.288	C14	-0.27,171	C14	-0.27,677
C15	-0.1976	C15	-0.19,613	C15	-0.20,977	C15	-0.21,412	C15	-0.20,505
C16	0.234,353	C16	0.237,978	C16	0.201,504	N16	-0.61,327	C16	0.205,578
N17	-0.60,375	C17	-0.20,395	C17	-0.19,118	C17	0.350,766	C17	-0.19,076
C18	-0.21,302	C18	-0.13,491	C18	-0.14,031	C18	0.20,196	C18	-0.14,112
C19	-0.13,764	C19	-0.05,245	C19	-0.05,067	C19	-0.18,991	C19	-0.05,172
C20	-0.05,417	C20	-0.13,596	C20	-0.14,427	C20	-0.13,686	C20	-0.14,443
C21	-0.13,841	C21	-0.19,095	C21	-0.20,445	C21	-0.04,355	C21	-0.20,482
C22	-0.19,017	Cl22	-0.0124	Cl22	-0.0148	C22	-0.13,972	Cl22	-0.02,566
Cl23	-0.01,879	N23	-0.40,828	H23	0.192,059	C23	-0.20,234	N23	-0.7412
C24	0.446,881	H24	0.202,034	N24	-0.37,062	Cl24	-0.05,475	C24	0.178,532
O25	-0.38,645	C25	0.534,589	C25	0.228,527	C25	0.185,935	N25	-0.47,786
C26	-0.56,613	C26	0.429,239	C26	0.429,075	N26	-0.48,041	H26	0.349,392
C27	0.219,359	O27	-0.34,199	S27	-0.16,274	H27	0.192,911	H27	0.342,203
C28	0.044,574	C28	-0.57,185	N28	-0.66,379	N28	-0.24,683	H28	0.370,277
N29	-0.74,756	O29	-0.35,088	O29	-0.33,839	C29	-0.55,178	H29	0.335,344
C30	0.459,905	N30	-0.70,697	C30	-0.5708	N30	-0.58,788	H30	0.168,043
O31	-0.39,513	C31	0.218,984	C31	0.232,072	H31	0.353,166	H31	0.183,264
O32	-0.42,247	N32	-0.43,888	N32	-0.44,627	H32	0.340,935	H32	0.147,791
C33	-0.49,481	H33	0.351,268	H33	0.352,189	H33	0.341,923	H33	0.157,868
C34	-0.09,933	H34	0.343,106	H34	0.344,334	H34	0.398,673	H34	0.157,611
C35	0.255,481	H35	0.335,774	H35	0.337,962	H35	0.170,853	H35	0.170,843
N36	-0.51,067	H36	0.37,662	H36	0.376,557	H36	0.357,989	H36	0.356,086
H37	0.194,727	H37	0.173,718	H37	0.181,424	H37	0.151,292	H37	0.33,612
H38	0.34,936	H38	0.143,045	H38	0.156,802	H38	0.161,612		
H39	0.341,389	H39	0.162,179	H39	0.164,064	H39	0.160,501		
H40	0.332,701	H40	0.159,742	H40	0.160,893	H40	0.168,682		
H41	0.375,474	H41	0.142,467	H41	0.170,276	H41	0.175,209		
H42	0.134,834	H42	0.180,319	H42	0.363,916	H42	0.177,795		
H43	0.336,476	H43	0.202,686	H43	0.352,245	H43	0.199,633		
H44	0.127,009	H44	0.216,714	H44	0.178,873	H44	0.344,945		
H45	0.154,897	H45	0.348,737	H45	0.203,918	H45	0.318,892		
H46	0.167,667	H46	0.344,657	H46	0.217,976				
H47	0.166,944								
H48	0.233,544								
H49	0.19,201								
H50	0.166,636								
H51	0.379,488								
H52	0.345,073								
H53	0.172,897								
H54	0.166,486								
H55	0.166,435								
H56	0.181,945								
H57	0.182,659								

Instead, they provide a molecular level interpretation of electronic softness, charge distribution, and probable interaction sites. Therefore, the computational results were interpreted together with the larvicidal, enzymatic, and oxidative stress data to rationalize the observed activity trend rather than to prove a direct biological target [49].

2.5. Structure-activity relationship analysis

Among the synthesized compounds, **11** demonstrated potent biological activity with a value measurement. The contribution of the carbamothioyl fragment in this compound appears to enhance the localization of reactive centers around the substituent-bearing region. Meanwhile, compound **7** showed effectiveness, requiring a concentration of 1000 μg/mL to achieve complete larval death (Table 3). The consistent decline in lethal concentration values (LC_{50}, LC_{90}, and LC_{95}) across all compounds over the 48-hour period underscores a clear cumulative toxic effect, establishing these hybrids as promising candidates for mosquito vector control. Compounds containing more electron donors with resonance-stabilizing structures appear to exhibit enhanced biochemical with antioxidant activity, as reflected by their lower LC_{50} or IC_{50} values. While **9** showed intermediate gaps, indicating a moderate degree of electronic stability and the target biological activity. Compound **13** is lower in EDG than **9**, so tested biological measurements decrease in compound **13**. In contrast, compound **15** showed relatively

weak inhibitory effects, with enzyme activity values close to those of the control group. The derivative shows increased activity because its chemical structure enables (Fig. 9).

3. Experimental

3.1. Preparation of silver nanoparticles for catalytic application

As a dispersion agent, 1.27 g of polyvinyl pyrrolidone (PVP) [50] was used. After dissolving 5.94 g of glucose in 15 mL of deionized H_2O and adding 0.96 g of NaOH to increase the reaction velocity, the mix was heated to 60 °C while being constantly stirred. Drop by drop, 0.01 M silver nitrate solution was added to the PVP solution. Following the addition of the $AgNO_3$ solution to reduce the silver ions (Ag^+) [51,52], for ten minutes, the mixture was further stirred. Centrifugation was used to separate the particles, and they were repeatedly cleaned with distilled water until no NO_3^- could be detected. At 80 °C, the particles were dried. Silver nanoparticles with a gray appearance were produced as powder [32]. Catalyst recycling was looked into, and it's important to show that our synthetic protocol is sustainable.

3.1.1. Characterization of silver nanoparticles

XRD; BRUKER D8 ADVANCED, utilizing CuKα radiation (λ = 1.5406 Å). Phase identification was achieved by analyzing diffraction patterns with the Joint Committee on Powder Diffraction Standards (JCPDS) reference standard. The study utilized FT-IR, Perkin Elmer Spectrum 1600, at room temperature in the 400–4000 cm^{-1} range. Scanning electron microscopy (JEOL JSM 5600) was used for microstructural examination. TEM Tecani 20 G2 experiments were carried out at 200 KV.

3.2. Materials and instruments

TLC was carried out employing $CHCl_3$:MeOH (9:1), and ethyl acetate:toluene (1:1) were the solvent systems utilized. Each M.P. was recorded using an uncorrected Stuart melting point instrument. Analytical spectroscopic techniques utilized for structure characterization were IR (Pye-Uniearn using the KEr wafer technique) at Mansoura University. At Zagazig University, NMR spectra were analyzed using DMSO-d_6 as a solvent at 400 MHz for ^{1}H NMR and 100 MHz for ^{13}C NMR. Also, at Mansoura University, NMR spectra were analyzed using DMSO-d_6 as a solvent at 500 MHz for ^{1}H NMR and 125 MHz for ^{13}C NMR. At the Regional Center for Mycology and Biotechnology, mass spectra were captured on the electron ionization (EI).

6-Aminouracil (l)

Compound **1** was sold commercially by Aldrich Chemical Company, Inc. [53].

5-Acetyl-6-aminouracil (3)

In our laboratory, it was manufactured. as a documented technique [54].

***N*-(6-(6-amino-2,4-dioxo-1,2,3,4-tetrahydropyrimidin-5-yl)-4-(4-chlorophenyl)-3-cyano-4*H*-pyran-2-yl)acetamide (5).**

A mix of **3** (0.001 mol) and active methylene, namely 4-chlorobenzylidene malononitrile (**4**) (0.001 mol), was refluxed in 30 mL AcOH along with a silver nanocatalyst for 6 h at 110 °C and filtered hot. The solid product was washed with cold H_2O, dried, and recrystallized from EtOH to give a pure compound as yellow crystals; yield 94.5%; M. P. = 186–188 °C. IR (KBr) υ cm^{-1}: 3456, 3360, 3185, 3159, 3064, 2850, 2211, 1649; ^{1}H NMR (400 MHz, δ, ppm): 2.40 (s, 3H, CH_3), 7.14 (s, 2H, NH_2, D_2O exchangeable), 7.64–7.66 (d, *J* = 8 Hz, 2H, Ar-H), 7.80 (s, 1H, CH), 7.93–7.95 (d, *J* = 8 Hz, 2H, Ar-H), 8.17 (s, 1H, CH), 10.01–10.64 (s, 3H, 3NH, D_2O exchangeable); ^{13}C NMR (100 MHz, δ, ppm): 31.5, 90.0, 107.3, 116.2, 129.4, 130.8, 131.7, 132.1, 136.9, 148.7, 149.3, 158.6, 162.5, 163.3, 196.4; MS (EI): *m/z* (intensity 100%): 402 (12) $[M + 2]^{+\cdot}$, 400 (12) $[M]^{+\cdot}$, 348 (100). Anal. calcd. For $C_{18}H_{14}ClN_5O_4$, %: C, 54.08; H, 3.53; N, 17.52; found: C, 54.19; H, 3.58; N, 17.87.

Ethyl-3-[(2-acetamido-6-(6-amino-2,4-dioxo-1,2,3,4-tetrahydropyrimidin-5-yl)-4-(4-chlorophenyl)-4*H*-pyran-3-yl)]-3-amino-2-cyanoacrylate (7).

Compound **5** (0.001 mol) and ethyl cyanoacetate (**6**) (0.001 mol) were combined with ethyl alcohol (10 mL) in the presence of Ag-NPs as a nanocatalyst and refluxed for 2.15 h at 78 °C. The resulting solid product was filtered, dried, and recrystallized from EtOH to yield **7** as yellow crystals after cooling to room temperature. Yield: 95.9%; M. P. = 256–258 °C. IR (KBr) υ cm^{-1}: 3450, 3408, 3191, 3101, 2855, 2211, 1741, 1650; ^{1}H NMR (400 MHz, δ, ppm): 1.18–1.22 (t, 3H, *J* = 8 Hz, –CH_2CH_3), 2.07 (s, 3H, CH_3), 4.12–4.18 (q, 2H, *J* = 8 Hz, –CH_2CH_3), 4.42 (s, 2H, NH_2), 7.21–7.23 (d, *J* = 8 Hz, 2H, Ar-H), 7.30–7.32 (d, *J* = 8 Hz, 2H, Ar-H), 7.44 (s, 1H, CH), 7.47 (s, 1H, CH), 7.68 (s, 2H, NH_2), 10.05 (s, 1H, NH), 10.77 (s, 1H, NH), 11.74 (s, 1H, NH); ^{13}C NMR (100 MHz, δ, ppm): 31.3, 34.3, 41.4, 48.2, 66.2, 112.9, 115.6, 125.2, 126.5, 127.0, 127.3, 127.5, 129.5, 131.4, 132.2, 148.3, 149.0, 150.7, 151.0, 151.1; MS (EI): *m/z* (intensity 100%): 515 (24) $[M + 2]^{+\cdot}$, 513 (32) $[M]^{+\cdot}$, 232 (100). Anal. calcd. for $C_{23}H_{21}ClN_6O_6$, %: C, 53.86; H, 4.13; N, 16.39; found: C, 53.92; H, 4.18; N, 16.47.

***N*-[6-(6-amino-2,4-dioxo-1,2,3,4-tetrahydropyrimidin-5-yl)-4-(4-chlorophenyl)-3-cyano-4*H*-pyran-2-yl)]-*N*-carbmoylacetamide (9)**

Compound **5** and urea (**8**) were combined with equal moles in 10 mL of absolute ethanol and heated under reflux for 4 h at 78 °C in the presence of Ag-NPs. The mixture was then cooled until it reached room temperature. After being filtered, dried, and recrystallized from ethanol, the solid product **9** was formed as yellow crystals. Yield: 93.8%; M. P. = 102–104 °C. IR (KBr) υ cm^{-1}: 3447, 3373, 3354, 3185, 3098, 2853, 2209, 1644; ^{1}H NMR (400 MHz, δ, ppm): 2.35 (s, 3H, CH_3), 7.14 (s, 2H, NH_2), 7.23 (s, 1H, CH), 7.32–7.34 (d, *J* = 8 Hz, 2H, Ar-H), 7.39 (s, 1H, CH), 7.49–7.51 (d, *J* = 8 Hz, 2H, Ar-H), 7.69 (s, 2H, NH_2), 10.02 (s, 1H, NH), 10.64 (s, 1H, NH); ^{13}C NMR (100 MHz, δ, ppm): 23.5, 25.3, 60.8,

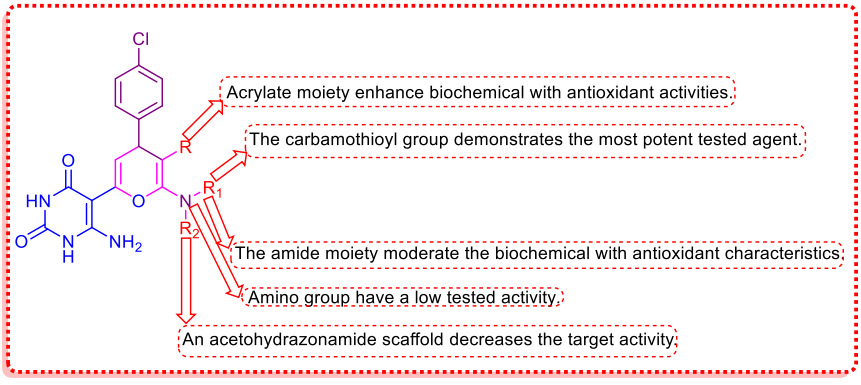

Fig. 9. Compounds' SAR graph.

98.3, 115.7, 128.3, 128.7, 129.4, 130.9, 132.8, 133.2, 150.2, 155.5, 160.1, 160.8, 163.3, 166.1; MS (EI): *m/z* (intensity 100%): 445 (16) $[M + 2]^{+\cdot}$, 443 (29) $[M]^{+\cdot}$, 71 (100). Anal. calcd. for $C_{19}H_{15}ClN_6O_5$, %: C, 51.53; H, 3.41; N, 18.98; found: C, 51.62; H, 3.63;

N, 18.95.

***N*-[6-(6-amino-2,4-dioxo-1,2,3,4-tetrahydropyrimidin-5-yl)-4-(4-chlorophenyl)-3-cyano-4*H*-pyran-2-yl)] -*N*-carbmothioylacetamide (11)**

In absolute ethyl alcohol (10 mL) with 0.001 mol of compound **5** and 0.001 mol of thiourea (**10**) and Ag-NPs, the combination was refluxed for 3.45 h at 78 °C. The reaction mix was cooled until it reached room temperature. The resultant solid **11** was purified from the ethanol, dried, and then recrystallized into yellow crystals. Yield: 94.5%; M. P. = 132–134 °C. IR (KBr) υ cm^{-1}: 3453, 3379, 3305, 3278, 3161, 3094, 2853, 2210, 1647; ^{1}H NMR (400 MHz, *δ*, ppm): 2.51 (s, 3H, CH_3), 7.31–7.33 (d, *J* = 8 Hz, 1H, CH), 7.39–7.41 (d, *J* = 8 Hz, 1H, CH), 7.65–7.67 (d, *J* = 8 Hz, 2H, Ar-H), 7.81 (s, 2H, NH_2), 7.94–7.96 (d, *J* = 8 Hz, 2H, Ar-H), 8.18 (s, 2H, NH_2), 10.01 (s, 1H, NH), 10.63 (s, 1H, NH); ^{13}C NMR (100 MHz, *δ*, ppm): 21.7, 22.3, 43.8, 107.3, 116.2, 127.4, 128.2, 128.3, 129.3, 130.8, 130.9, 131.6, 136.8, 149.2, 162.5, 163.2, 183.8; MS (EI): *m/z* (intensity 100%): 461 (21) $[M + 2]^{+\cdot}$, 459 (9) $[M]^{+\cdot}$, 312 (100). Anal. calcd. for $C_{19}H_{15}ClN_6O_4S$, %: C, 49.73; H, 3.29; N, 18.31; found: C, 49.81; H, 3.35; N, 18.36.

***N*-[6-(6-amino-2,4-dioxo-1,2,3,4-tetrahydropyrimidin-5-yl)-4-(4-chlorophenyl)-3-cyano-4*H*-pyran-2-yl)] acetohydrazonamide (13)**

Compound **5** and hydrazine hydrate (**12**) were combined in equal moles in 10 mL of ethyl alcohol and heated under reflux for 2 h at 78 °C using a silver nanocatalyst. The reaction mix was poured onto cold H_2O (10 mL) after cooling to room temperature. Yellow crystals of the resultant product **13**, which was filtered, dried, and recrystallized from methanol, were produced. Yield: 96.3%; M.P. = 158–160 °C. IR (KBr) υ cm^{-1}: 3403, 3332, 3186, 3049, 2854, 2220, 1647; ^{1}H NMR (500 MHz, *δ*, ppm): 3.34 (s, 3H, CH_3), 7.33 (s, 1H, CH), 7.45–7.47 (d, *J* = 9 Hz, 2H, Ar-H), 7.56 (s, 4H, $2NH_2$, D_2O exchangeable), 7.88–7.90 (d, *J* = 8 Hz, 2H, Ar-H), 8.71 (s, 1H, CH), 10.04 (s, 1H, NH, D_2O exchangeable), 10.69 (s, 1H, NH, D_2O exchangeable), 11.11 (s, 1H, NH, D_2O exchangeable); ^{13}C NMR (125 MHz, *δ*, ppm): 22.8, 25.3, 52.5, 116.3, 127.4, 127.7, 128.9, 129.1, 129.4, 129.5, 130.0, 132.6, 136.0, 160.7, 164.1; MS (EI): *m/z* (intensity 100%): 416 (44) $[M + 2]^{+\cdot}$, 414 (25) $[M]^{+\cdot}$, 312 (100). Anal. calcd. for $C_{18}H_{16}ClN_7O_3$, %: C, 52.24; H, 3.90; N, 23.69; found: C, 52.34; H, 3.94; N, 23.73.

2-Amino-6-[(6-amino-2,4-dioxo-1,2,3,4-tetrahydropyrimidin-5-yl)-4-(4-chlorophenyl)] -4*H*-pyran-3-carbonitrile (15).

Compound **5** (0.001 mol) and formic acid (**14**) (0.001 mol) were combined and heated in reflux for 1 h at 78 °C in the presence of Ag-NPs as a nanocatalyst. The mixture was cooled to RT. The resultant precipitate **15** was dried, filtered, and recrystallized as buff crystals from ethanol. Yield: 97.1%; M.P. = 212–214 °C. IR (KBr) υ_{max} cm^{-1}: 3483, 3455, 3373, 3305, 3241, 3156, 3062, 2852, 2212, 1658; ^{1}H NMR (400 MHz, *δ*, ppm): 7.28–7.30 (d, *J* = 8 Hz, 1H, CH), 7.46–7.48 (d, *J* = 8 Hz, 1H, CH), 7.64–7.66 (d, *J* = 8 Hz, 2H, Ar-H), 7.80 (s, 2H, NH_2), 7.93–7.95 (d, *J* = 8 Hz, 2H, Ar-H), 8.17 (s, 2H, NH_2), 10.96 (s, 1H, NH), 11.49 (s, 1H, NH); ^{13}C NMR (100 MHz, *δ*, ppm): 88.4, 98.2, 107.3, 115.3, 116.2, 127.7, 129.3, 129.5, 130.8, 131.6, 132.2, 133.0, 136.8, 149.2, 162.5, 163.0; MS (EI): *m/z* (intensity 100%): 360 (33) $[M + 2]^{+\cdot}$, 358 (34) $[M]^{+\cdot}$, 296 (100). Anal. calcd. for $C_{16}H_{12}ClN_5O_3$, %: C, 53.72; H, 3.38; N, 19.58; found: C, 53.84; H, 3.41; N, 19.66.

3.3. Larvicidal bioassay on mosquitoes

3.3.1. Laboratory rearing of culex pipiens

Culex pipiens larvae were reared under laboratory insectary conditions at 27 ± 2 °C and 70–80% relative humidity with a photoperiod of 12:12 h (light:dark). Larvae were reared in trays containing dechlorinated water and supplied daily with a diet consisting of powdered fish food (Tetramin fish food) and yeast. Pupae were collected and transferred into cups containing clean water inside screened cages for adult emergence. The emergent adults received a 10% sucrose solution for their maintenance, while the female mosquitoes needed blood meals at regular intervals to produce their eggs. The researchers carried out all tests in controlled lab environments that followed the standard mosquito breeding methods established by Kauffman *et al.* (2017) [55] and Meuti *et al.* (2023) [56].

3.4. Mosquito larvicidal and biochemical assays

3.4.1. Larvicidal and biochemical assays

The effectiveness of larvicides against *Cx. pipiens* 3rd instar larvae was tested following the WHO larval bioassay guidelines, which were established in 2005 [38]. Six different concentrations were tested (25, 50, 125, 250, 500, and 1000 μg/mL) that they prepared by dissolving the substances in distilled H_2O. The researchers used a setup where twenty larvae existed in a 250 mL solution for every concentration while they conducted experiments three times. Temephos was used at 0.25 μg/mL as the positive control, which they administered according to standard larvicidal protocols detailed by Cetin *et al.* (2006) [57], while they used distilled water as the negative control. The researchers documented mortality rates after 24 and 48 h of exposure while they presented results as mean values with standard deviation. Previous studies have demonstrated that both synthetic and natural compounds can exhibit significant larvicidal activity against mosquito larvae, including *Cx. pipiens* [58].

3.5. Biochemical and oxidative stress analysis

3.5.1. Measuring the biochemical activities of enzymes

Crude tissue homogenates were created from 70 mosquito larvae by grinding specific tissue weights together with ice-cold sodium phosphate buffer, which had two different pH levels. The researchers subjected homogenates to centrifugation at 10,000 rpm for 10 min. inside a 4 °C environment, which allowed them to gather supernatants for their enzymatic tests. The Ellman colorimetric method [59], which is commonly used in insect toxin research, measured acetylcholinesterase activity. The researchers used a naphthyl acetate-based microplate assay to measure esterase activities (*α*- and *β*-esterase) according to established protocols that describe insect enzyme testing procedures [60,61]. Developed spectrophotometric techniques were used to examine GABA-transaminase and amylase activities, which scientists commonly use to study insect biochemical functions [62]. Enzyme activities were presented in units, which were calculated by dividing total enzyme activity by total protein weight (U/mg protein). The Bradford method established total protein content, which researchers used to determine protein amount [63].

3.6. Oxidative stress biomarkers

The physiological effects of the tested compounds on mosquito larvae were evaluated by measuring various oxidative stress and antioxidant defense biomarkers in the larval homogenates. The study used standard spectrophotometric methods, which are typically used in insect toxicology research, to measure the activity of three antioxidant enzymes, SOD, CAT, and GST [64–66]. The study measured reduced glutathione content and oxidative damage indicators, which included LPO and TPC levels, through established biochemical procedures [67–69]. The obtained results were expressed relative to protein content and used to assess the oxidative stress status and antioxidant response of *Culex pipiens* larvae after treatment with the tested compounds.

3.7. Antioxidant assay using DPPH

The antioxidant activity of five synthesized compounds (**7, 9, 11, 13,**

and **15**) was evaluated using the DPPH radical scavenging assay. This method is widely employed for the in vitro assessment of free radical scavenging capacity and electron or hydrogen donating potential of bioactive compounds [70]. In this assay, a series of different concentrations of each tested compound, as well as ascorbic acid, were prepared and individually mixed with a freshly prepared DPPH solution in methanol. The reaction mix was incubated in the dark at RT for a fixed time to avoid photodegradation of the DPPH radical and to ensure the stability of the reaction system. A UV–visible spectrophotometer was used to assess the decrease in absorbance at 540 nm following incubation. This wavelength corresponds to the reduction of the purple DPPH radical to its yellow non-radical state upon antioxidant activation. To assure accuracy, reproducibility, and statistical reliability, every experiment was run in triplicate. By comparing the treated and control samples, the mean absorbance values were utilized to determine the percentage of DPPH radical scavenging activity. To evaluate the dose–response behavior, the percentage inhibition was plotted against the corresponding concentrations for each compound and for ascorbic acid across the tested conc. range. The antioxidant potency was expressed in terms of IC_{50} values, defined as the concentration required to inhibit 50% of DPPH radical activity. Nonlinear regression analysis based on a four-parameter logistic (4PL) framework was used to determine IC_{50} values, which provides a robust and accurate description of sigmoidal dose–response relationships. The obtained IC_{50} values allowed direct comparison between the reference standard and the synthesized compounds, demonstrating variations in antioxidant efficiency depending on structural differences among the tested molecules. Overall, this assay provides a reliable and reproducible method for evaluating and comparing the free radical scavenging activity of ascorbic acid and the synthesized compounds under standardized experimental conditions [71].

3.8. Statistical analysis

Every experiment was conducted in triplicate, and the mean ± standard deviation was used to express the results. SPSS software version 23.0 (IBM Corp., Armonk, NY, USA) was used for all statistical analyses. Before subjecting data to parametric analyses, the core statistical assumptions were thoroughly evaluated; the normality of data distribution was verified using the Shapiro-Wilk test, and the homogeneity of variances was assessed via Levene's test. Differences among treatment groups were analyzed using a One-way Analysis of Variance (ANOVA), followed by Tukey's HSD post-hoc test for multiple pairwise comparisons ($P < 0.05$). For larvicidal bioassays, the percentage of larval mortality in the control groups was observed to be 0%, and thus no further mortality correction (via Abbott's formula) was required. Lethal concentration values (LC_{50} and LC_{90}), 95% confidence intervals, regression equations, and chi-square (χ^2) values were computed through Probit analysis using the integrated statistical bioassay tools within the SPSS software version 23.0, following Finney (1971) [72]. The goodness-of-fit of the Probit model was assessed using the chi-square (χ^2) test, where a non-significant χ^2 ($P > 0.05$) indicates adequate model fit. In cases where significant χ^2 values ($P < 0.05$) were observed, this suggests some heterogeneity in the data, which may result from steep concentration-response curves or limited variability between doses. Despite this, the LC estimates remain reliable, as they are derived from the established regression model and are supported by clear concentration-dependent mortality trends observed experimentally.

3.9. Computational analysis

3.9.1. Fukui function and dual descriptor

All chemical calculations were carried out using Gaussian 09 W software suite [73]. The molecular geometries of compounds **7, 9, 11, 13**, and **15** were fully optimized using density functional theory at the B3LYP/6–311++G(d,p) level. Calculations were performed for isolated molecules in the gas phase unless otherwise stated [74]. The neutral molecules were treated as closed shell singlet systems with charge = 0 and multiplicity = 1 [75]. Geometry optimizations were performed using default Gaussian convergence criteria [76]. Frequency calculations were performed at the same level of theory to confirm the optimized structures correspond to true minima on the potential energy surface [77]. The optimized neutral geometries were then used for other analyses.

The local reactivity of compounds **7, 9, 11, 13**, and **15** was evaluated using condensed Fukui function analysis based on DFT calculations. Geometry optimization and single-point calculations for the neutral, cationic, and anionic species were carried out at the level using the POP=NBO keyword [78]. NBO-derived atomic charges were then used to calculate the condensed FUKUI descriptors with UCA-FUKUI v2.0 interface [43]. The calculated Fukui descriptors f^+, f^-, and f^0 values, obtained from NBO-derived atomic charges, were used to predict the preferred sites for electrophilic, nucleophilic, and radical attack, respectively.

3.9.2. Frontier molecular orbital analysis and global reactivity descriptors

Frontier Molecular Orbital analysis (FMO) was conducted for compounds **7, 9, 11, 13**, and **15** using their DFT-optimized neutral structures at the B3LYP/6–311++G(d,p) level. The Highest Occupied Molecular Orbital (HOMO) and Lowest Unoccupied Molecular Orbital (LUMO) distributions were visualized with GaussView 5.0, and the HOMO-LUMO energy gap (ΔE) was calculated to assess molecular stability and electronic reactivity. A large energy gap indicates that the compound is more stable, while the small gap indicates that the compound has more chemical reactivity [79].

Global reactivity descriptors were also calculated from the HOMO and LUMO energies, including ionization potential (IP), electron affinity (Ea), chemical potential (μ), chemical hardness (η), softness (S), and electronegativity (χ). These parameters were used to describe the electronic stability, charge-transfer tendency, and possible interaction behavior of the synthesized compounds.

3.9.3. Map of the molecular electrostatic potential

MEP was used to investigate the electronic behavior and the molecular reactivity of the synthesized compounds **7, 9, 11, 13**, and **15**. It facilitates the interpretation of the preferred sites for nucleophilic and electrophilic attacks. In the MEP, surface areas colored in red represent areas of high electron density, suggesting these sites for electrophilic attack, whereas blue-colored regions represent electron-poor sites that are more favorable for nucleophilic attack [80]. These maps also provide useful information for predicting potential non-covalent interaction sites within the studied compounds.

3.9.4. Mulliken population analysis

Atomic charge distributions for compounds **7, 9, 11, 13**, and **15** were evaluated using Mulliken population analysis at the same DFT level described above. This charge analysis was used to examine the electronic distribution over the molecular framework and to identify atoms with relatively electron-rich or electron-deficient character.

4. Conclusion

This paper successfully studied the optimization of pyran-functionalized pyrimidinone moieties, starting from compound **5**, based on nanotechnology support. The incorporation of nanomaterials, particularly Ag-NPs, played a crucial function in improving reaction efficiency and product yield. The present study demonstrates that the synthesized pyran-pyrimidine hybrids possess potent larvicidal activity against *Culex pipiens*, characterized by a clear concentration and time-dependent response. The biological efficacy of these compounds is attributed to a multi-target mechanism of action. Among the tested derivatives, compound **11** emerged as the most potent candidate,

recording the lowest LC_{50} and LC_{90} values and achieving total mortality at higher concentrations. The biochemical assessment revealed a significant disruption of essential larval systems, including the inhibition of neurological enzymes (AChE and esterases) and digestive enzymes (protease and phosphatases), which impairs synaptic transmission and nutrient metabolism. Furthermore, the compounds triggered severe oxidative stress, evidenced by the depletion of antioxidant defenses (SOD, CAT, GST, and GSH) and a concomitant rise in oxidative damage markers (LPO and TPC). These results suggest the potential use of pyran-pyrimidinone compounds as promising lead compounds for the development of novel, multifunctional mosquito control agents. The study demonstrates that targeting multiple physiological systems simultaneously is a promising strategy for addressing the growing challenge of insecticide resistance in vector populations. However, it is important to note that the current findings are based on in vitro biological assays and biochemical evaluations. Therefore, further studies, including environmental safety assessments, non-target organism toxicity studies, field validation trials, and resistance evolution analyses, are needed before any practical application or direct comparison with conventional insecticides can be recommended. Within these limitations, compound **11** emerges as a highly promising candidate for further refinement and advanced preclinical development. Compound **11**, exhibiting the highest potency among the tested derivatives and showing activity comparable to the reference standard ascorbic acid, highlighting the potential of these compounds as promising antioxidant candidates for further pharmacological investigation. The DFT findings indicate the electronic behavior of the synthesized compounds. Compound **11** showed the smallest HOMO-LUMO gap (4.040 eV) and the highest softness (0.495 eV^{-1}), indicating that it is the most electronically flexible and the most preferred for charge transfer interactions, while compound **15** exhibited the largest gap (4.819 eV) and the highest chemical hardness (2.410 eV), suggesting higher kinetic stability and low reactivity. The local reactivity analyses showed that the *O* and *N* atoms are the main electron-donating sites, while the polarized carbon atoms are more susceptible to nucleophilic attack. These findings highlight hybrid **11** as a promising candidate for further optimization as a multi-functional mosquito control and antioxidant agent.

Funding information

No fund.

CRediT authorship contribution statement

Basant Farag: Formal analysis, Funding acquisition, Investigation, Project administration, Resources, Software, Supervision, Writing – original draft, Writing – review & editing. **Mohamed Abdel-Haleem:** Methodology, Software, Writing – original draft, Writing – review & editing. **Sampath Chinnam:** Supervision, Validation, Visualization, Writing – original draft, Writing – review & editing. **Ismail A. Elhaty:** Resources, Software, Supervision, Validation, Visualization, Writing – original draft, Writing – review & editing. **Shaimaa Abozeid:** Methodology, Writing – original draft, Writing – review & editing. **Mohammed E. Gad:** Methodology, Writing – original draft, Writing – review & editing. **Aamer Saeed:** Software, Supervision, Validation, Visualization, Writing – original draft, Writing – review & editing. **Abdelfattah Selim:** Conceptualization, Data curation, Writing – original draft, Writing – review & editing. **Mohamed M. Baz:** Methodology, Writing – original draft, Writing – review & editing.

Declaration of competing interest

The authors declare that none of their known financial or personal conflicts would have appeared to have affected the findings of this investigation.

Acknowledgement

The authors express their sincere gratitude for the support of this work.

Supplementary materials

Supplementary material associated with this article can be found, in the online version, at doi:10.1016/j.molstruc.2026.147405.

Data availability

Data will be made available on request.

References

[1] G. Benelli, H. Mehlhorn, Declining malaria, rising of dengue and Zika virus: insights for mosquito vector control, Parasitol. Res. 115 (2016) 1747–1754, https://doi.org/10.1007/s00436-016-4971-z.
[2] A. Farajollahi, D.M. Fonseca, L.D. Kramer, A.M. Kilpatrick, Bird biting" mosquitoes and human disease: a review of the role of *Culex pipiens* complex mosquitoes in epidemiology, Infect. Genet. Evol. 11 (2011) 1577–1585, https://doi.org/10.1016/j.meegid.2011.08.013.
[3] R.E. Harbach, *Culex pipiens*: species versus species complex–taxonomic history and perspective, JAMCA 28 (2012) 10–23, https://doi.org/10.2987/8756-971X-28.4.10.
[4] A.T. Ciota, West Nile virus and its vectors, Curr. Opin. Insect Sci. 22 (2017) 28–36, https://doi.org/10.1016/j.cois.2017.05.002.
[5] A. Nebbak, L. Almeras, P. Parola, I. Bitam, Mosquito vectors (Diptera: Culicidae) and mosquito-borne diseases in North Africa, Insects 13 (2022) 962, https://doi.org/10.3390/insects13100962.
[6] M. Garbuio, K.J.S. Silva, L.D. Dias, V.S. Bagnato, A.R. Lima, Photodynamic inactivation for the control of disease-transmitting vectors: mechanisms, photosensitizers, and biological targets-a review, Photochem. Photobiol. 278 (2026) 113434, https://doi.org/10.1016/j.jphotobiol.2026.113434.
[7] J. Hemingway, H. Ranson, Insecticide resistance in insect vectors of human disease, Annu. Rev. Entomol. 45 (2000) 371–391, https://doi.org/10.1146/annurev.ento.45.1.371.
[8] J. Hemingway, N.J. Hawkes, L.M.C. Carroll, H. Ranson, The molecular basis of insecticide resistance in mosquitoes, Insect Biochem. Mol. Biol. 34 (2004) 653–665, https://doi.org/10.1016/j.ibmb.2004.03.018.
[9] P.M. Ngegba, M.Z. Khalid, W. Jiang, G. Zhong, An overview of insecticide resistance mechanisms, challenges, and management strategies in Spodoptera frugiperda, Crop Prot. 197 (2025) 107322, https://doi.org/10.1016/j.cropro.2025.107322.
[10] R.S. Keri, K.M. Hosamani, R.V. Shingalapur, M.H. Hugar, Analgesic, anti-pyretic and DNA cleavage studies of novel pyrimidine derivatives of coumarin moiety, Eur. J. Med. Chem. 45 (2010) 2597–2605, https://doi.org/10.1016/j.ejmech.2010.02.048.
[11] Y. Zhang, X. Liu, C. Zhang, Y. Li, G. Zhang, Z. Du, FDA-approved pyrimidine-containing drugs: synthesis and clinical application, Med. Res. Rev. 46 (2026) 713–748, https://doi.org/10.1002/med.70027.
[12] G. Shabir, A. Saeed, A. Siyadatpanah, R. Javed, M. Irfan, B. Farag, S.M. Gomha, H. R. El-Seedi, S. Desale, Update on FDA-approved fluorinated drugs (2023–2025): structural chemistry, polypharmacology, and antiparasitic potential, Results Chem. 29 (2026) 103715, https://doi.org/10.1016/j.rechem.2026.103715.
[13] W. Shehta, N.A. Alsaiari, B. Farag, M.M. Abdel-Aziz, S. Youssif, S.M. Elfeky, S. El-Kalyoubi, N.A. Osman, Synthesis, in vitro and in silico molecular docking studies of novel phthalimide–pyrimidine hybrid analogues to thalidomide as potent antitubercular agents, SynOpen 9 (2025) 73–83, https://doi.org/10.1055/s-0043-1775424.
[14] M. Alhilal, S. Alhilal, S.M. Gomha, B. Farag, I. Sabancilar, S.A. Ouf, Biological evaluation and molecular docking studies of novel aza-acyclic nucleosides as putative antimicrobial, anticancer, and antioxidant agents, BMC Chem. 19 (2025) 255, https://doi.org/10.1186/s13065-025-01623-x.
[15] S. Kumar, B. Saroha, G. Kumar, E. Lathwal, S. Kumar, B. Parshad, M. Kumari, N. Kumar, M.M. Mphahlele-Makgwane, P.R. Makgwane, Recent developments in nanocatalyzed green synthetic protocols of biologically potent diverse *O*-heterocycles—a review, Catalysts 12 (2022) 657, https://doi.org/10.3390/catal12060657.
[16] G.G. El-Bana, M.A. Salem, M.H. Helal, O. Alharbi, M.A. Gouda, A review on the recent multicomponent synthesis of 4*H*-pyran derivatives, Mini-Rev. Org. Chem. 21 (2024) 73–91, https://doi.org/10.2174/1570193X19666220527163846.
[17] R. Pavela, Essential oils for the development of eco-friendly mosquito larvicides: a review, Ind. Crops Prod. 76 (2015) 174–187, https://doi.org/10.1016/j.indcrop.2015.06.050.
[18] G. Benelli, Research in mosquito control: current challenges for a brighter future, Parasitol. Res. 114 (2015) 2801–2805, https://doi.org/10.1007/s00436-015-4586-9.
[19] M. Chamani, M.R. Dadpour, Z. Dehghanian, S. Panahirad, A.C. Bouket, T. Oszako, S. Kumar, From digestion to detoxification: exploring plant metabolite impacts on

insect enzyme systems for enhanced pest control, Insects 16 (2025) 392, https://doi.org/10.3390/insects16040392.
[20] G.W. Felton, C.B. Summers, Antioxidant systems in insects, Arch. Insect Biochem. Physiol. 29 (1995) 187–197, https://doi.org/10.1002/arch.940290208.
[21] İ. Gulcin, S. Alwasel, DPPH radical scavenging assay, Processes 11 (2023) 2248, https://doi.org/10.3390/pr11082248.
[22] A.B. Sultan, M.I. Abdelglil, A.A. Mohamed, E.M. Haggag, G. El-Akabawy, D. K. Rawy, A.A. Ibrahim, K. Haidar, N. Foda, M. Abdel-Haleem, Integrated study on kaempferol's efficacy and mechanism of action: targeting *Escherichia coli* biofilms and colon cancer pathways alongside oxidative stress regulation, Chem. Pap. 80 (2026) 6431–6448, https://doi.org/10.1007/s11696-026-04775-9.
[23] L. Lonardi, C. Lew-Tong, B.D. Miranda, C.V. Shanthamani, E. Li, B. Sahukari, H. Poddar, K. Satheesh, U. Chadha, Toward a circular nanotechnology for biofuels: integrating sustainable synthesis, recovery, and performance optimization, Mater. Res. 41 (2026) 340–360, https://doi.org/10.1557/s43578-025-01709-1.
[24] L.M. De Coen, T.S.A. Heugebaert, D. Garcia, C.V. Stevens, Synthetic entries to and biological activity of pyrrolopyrimidines, Chem. Rev. 116 (2016) 80–139, https://doi.org/10.1021/acs.chemrev.5b00483.
[25] A. Alsharif, M. Allahyani, A. Aljuaid, A.A. Alsaiari, M.M. Almehmadi, M. Asif, Diverse pharmacological potential of various substituted pyrimidine derivatives, Curr. Org. Chem. 27 (2023) 1779–1798, https://doi.org/10.2174/0113852728266665231101112129.
[26] E. Zarenezhad, M. Farjam, A. Iraji, Synthesis and biological activity of pyrimidines-containing hybrids: focusing on pharmacological application, J. Mol. Struct. 1230 (2021) 129833, https://doi.org/10.1016/j.molstruc.2020.129833.
[27] B. Mehta, M. Chhajlani, B. Shrivastava, Green synthesis of silver nanoparticles and their characterization by XRD, in: Journal of Physics.: Conference Series 836, 2017 012050, https://doi.org/10.1088/1742-6596/836/1/012050. IOP Publishing.
[28] N. Vigneshwaran, N.M. Ashtaputre, P.V. Varadarajan, R.P. Nachane, K. M. Paralikar, R.H. Balasubramanya, Biological synthesis of silver nanoparticles using the fungus Aspergillus flavus, Mater. Lett. 61 (2007) 1413–1418, https://doi.org/10.1016/j.matlet.2006.07.042.
[29] S. Basavaraja, S.D. Balaji, A. Lagashetty, A.H. Rajasab, A. Venkataraman, Extracellular biosynthesis of silver nanoparticles using the fungus Fusarium semitectum, Mater. Res. Bull. 43 (2008) 1164–1170, https://doi.org/10.1016/j.materresbull.2007.06.020.
[30] D. Balaji, S. Basavaraja, R. Deshpande, D.B. Mahesh, B.K. Prabhakar, A. Venkataraman, Extracellular biosynthesis of functionalized silver nanoparticles by strains of Cladosporium cladosporioides fungus, Colloids Surf. B: Biointerfaces 68 (2009) 88–92, https://doi.org/10.1016/j.colsurfb.2008.09.022.
[31] L. Jaidev, G. Narasimha, Fungal mediated biosynthesis of silver nanoparticles, characterization and antimicrobial activity, Colloids Surf. B: Biointerfaces 81 (2010) 430–433, https://doi.org/10.1016/j.colsurfb.2010.07.033.
[32] A.S. Lanje, S.J. Sharma, R.B. Pode, Synthesis of silver nanoparticles: a safer alternative to conventional antimicrobial and antibacterial agents, J. Chem. Pharm. Res. 2 (2010) 478–483.
[33] M. Zhou, Z. Wei, H. Qiao, L. Zhu, H. Yang, T. Xia, Particle size and pore structure characterization of silver nanoparticles prepared by confined arc plasma, J. Nanomater. 2009 (2009) 968058, https://doi.org/10.1155/2009/968058.
[34] W. Shehta, F. Agili, B. Farag, S.A. Said, S. Youssif, M.E. Abdraboh, S. El-Kalyoubi, Design, synthesis and antitumor activity of novel pyran-functionalized uracil derivatives: docking studies, Future Med. Chem. 15 (2023) 421–436, https://doi.org/10.4155/fmc-2022-0279.
[35] K.E. Anwer, G.H. Sayed, B.M. Essa, A.A. Selim, Green synthesis of highly functionalized heterocyclic bearing pyrazole moiety for cancer-targeted chemo/radioisotope therapy, BMC Chem. 17 (2023) 139, https://doi.org/10.1186/s13065-023-01053-7.
[36] E.A. Ghaith, A.B. Abdallah, A.A. El-Sawi, G.G. El-Bana, Ultrasound-assisted utility of 1,2,4-triazole as a multisite-sequential scaffold to construct different heterocycles, accredited by molecular modeling and electrochemical studies, Heterocycl. Chem. 62 (2025) 1863–1875, https://doi.org/10.1002/jhet.70003.
[37] G. Benelli, F. Maggi, R. Pavela, K. Murugan, M. Govindarajan, B. Vaseeharan, R. Petrelli, L. Cappellacci, S. Kumar, A. Hofer, M.R. Youssefi, A.A. Alarfaj, J. S. Hwang, A. Higuchi, Mosquito control with green nanopesticides: towards the One Health approach? A review of non-target effects, Environ. Sci. Pollut. Res. 25 (2018) 10184–10206, https://doi.org/10.1007/s11356-017-9752-4.
[38] M. Larvicides, Guidelines for Laboratory and Field Testing of Mosquito Larvicides, Google Scholar, 2005.
[39] H.S. Kareem, A. Ariffin, N. Nordin, T. Heidelberg, A. Abdul-Aziz, K.W. Kong, W. A. Yehye, Correlation of antioxidant activities with theoretical studies for new hydrazone compounds bearing a 3,4,5-trimethoxy benzyl moiety, Eur. J. Med. Chem. 103 (2015) 497–505, https://doi.org/10.1016/j.ejmech.2015.09.016.
[40] M. Okram, R. Bharti, R. Sharma, M. Verma, R. Bansal, Microwave-assisted Cr_2O_3 nanoparticle-catalyzed synthesis of 2-amino-4*H*-chromenes: evaluation of antioxidant, corrosion inhibition, and molecular docking studies, Res. Chem. Intermed. 51 (2025) 6049–6086, https://doi.org/10.1007/s11164-025-05731-0.
[41] M.P. Parmar, R.M. Vala, H.M. Patel, Importance of hybrid catalysts toward the synthesis of 5*H*-Pyrano[2,3-*d*]pyrimidine-2-ones/2,4-diones (Thiones), ACS Omega 8 (2023) 1759–1816, https://doi.org/10.1021/acsomega.2c05349.
[42] A. Pandit, A. De, A.S. Palakkal, S. Kundu, S. Neogi, Antagonistically functionalized cobalt-organic framework enabling bifunctional water splitting and one-pot synthesis of bioactive 4*H*-Pyrans via synergistic catalysis, Small 22 (2026) e14442, https://doi.org/10.1002/smll.202514442.
[43] J. Sánchez-Márquez, D. Zorrilla, A. Sánchez-Coronilla, D.M. Santos, J. Navas, C. Fernández-Lorenzo, R. Alcántara, J. Martín-Calleja, Introducing "UCA-FUKUI" software: reactivity-index calculations, Mol. Model. 20 (2014) 2492, https://doi.org/10.1007/s00894-014-2492-1.
[44] S. Soni, K. Patil, S. Vishwakarma, R. Yadav, P.R. Murumkar, R. Kadu, Exploring the antimicrobial landscape of carbazole derivatives through integration of computational and experimental approaches, Discover Chem. 3 (2026) 149, https://doi.org/10.1007/s44371-026-00599-4.
[45] P. Geerlings, F. De Proft, W. Langenaeker, Conceptual density functional theory, Chem. Rev. 103 (2003) 1793–1874, https://doi.org/10.1021/cr990029p.
[46] B.A. Al Jahdaly, Electrochemical and DFT insights into 2-amino-4-(4-hydroxy-3-methoxyphenyl)-7-methyl-4*H*-chromene-3-carbonitrile: an innovative strategy for antibacterial activity and corrosion protection of carbon steel, RSC Adv. 14 (2024) 24039–24054, https://doi.org/10.1039/D4RA03785E.
[47] S. Ranjbar, P. Sadeghian, S. Khademian, M. Emami, Z.P. Jahromi, S.H. Mirmajidi, F. Zare, Y. Ghasemia, M. Negahdaripoura, M. Khoshneviszadeh, 5-Oxo-dihydropyranopyran derivatives as anti-proliferative agents; synthesis, biological evaluation, molecular docking, MD simulation, DFT, and in-silico pharmacokinetic studies, Heliyon 10 (2024) e29850, https://doi.org/10.1016/j.heliyon.2024.e29850.
[48] S. Gavale, S. Vishwakarma, S. Soni, S. Pathan, R. Yadav, P.R. Murumkar, R. Kadu, Synergistic exploration of thiazole derivatives: synthesis, antimicrobial activity and computational insights, J. Mol. Struct. 1333 (2025) 141772, https://doi.org/10.1016/j.molstruc.2025.141772.
[49] S. Soni, K. Patil, S. Gavale, S. Pathan, R. Yadav, P.R. Murumkar, R. Kadu, Exploring Oxazolidinone scaffolds for future antibiotics: synthesis and computational insights with DFT, docking, ADME and MD simulation, JCAMD 39 (2025) 58, https://doi.org/10.1007/s10822-025-00634-z.
[50] M. Zannotti, V. Vicomandi, A. Rossi, M. Minicucci, S. Ferraro, L. Petetta, R. Giovannetti, Tuning of hydrogen peroxide etching during the synthesis of silver nanoparticles. An application of triangular nanoplates as plasmon sensors for Hg^{2+} in aqueous solution, J. Mol. Liq. 309 (2020) 113238, https://doi.org/10.1016/j.molliq.2020.113238.
[51] Y. Liu, F. Li, Z. Guo, Y. Xiao, Y. Zhang, X. Sun, T. Zhe, Y. Cao, L. Wang, Q. Lu, J. Wang, Silver nanoparticle-embedded hydrogel as a photothermal platform for combating bacterial infections, Chem. Eng. J. 382 (2020) 122990, https://doi.org/10.1016/j.cej.2019.122990.
[52] K.B. Teodoro, F.M. Shimizu, V.P. Scagion, D.S. Correa, Ternary nanocomposites based on cellulose nanowhiskers, silver nanoparticles and electrospun nanofibers: use in an electronic tongue for heavy metal detection, Sens. Actuators B: Chem. 290 (2019) 387–395, https://doi.org/10.1016/j.snb.2019.03.125.
[53] S.S. Chavan, R.U. Shelke, M.S. Degani, Carboxylic acid-catalyzed one-pot synthesis of cyanoacetylureas and their cyclization to 6-aminouracils in guanidine ionic liquid, Monatsh. Für Chem. 144 (2013) 399–403, https://doi.org/10.1007/s00706-012-0810-9.
[54] J.L. Shim, R. Niess, A.D. Broom, Acylation of some 6-aminouracil derivatives, JOC 37 (1972) 578–581, https://doi.org/10.1021/jo00969a013.
[55] E. Kauffman, A. Payne, M.A. Franke, M.A. Schmid, E. Harris, L.D. Kramer, Rearing of *Culex spp.* and Aedes spp. mosquitoes, Bio-protoc 7 (2017), https://doi.org/10.21769/BioProtoc.2542 e2542-e2542.
[56] M.E. Meuti, A. Siperstein, M. Wolkoff, Rearing and maintaining a *Culex* colony in the laboratory, Cold Spring Harb. Protoc. 2023 (2023), https://doi.org/10.1101/pdb.prot108080 pdb. prot108080.
[57] H. Cetin, A. Yanikoglu, O. Kocak, J.E. Cilek, Evaluation of temephos and chlorpyrifos-methyl against *Culex pipiens* (Diptera: Culicidae) larvae in septic tanks in Antalya, Turkey, Med. Entomol. 43 (2006) 1195–1199, https://doi.org/10.1093/jmedent/43.6.1195.
[58] H.E. Zahran, M. D, H.K. Abou-Taleb, S.A. Abdelgaleil, Adulticidal, larvicidal and biochemical properties of essential oils against *Culex pipiens L*, J. Asia-Pac. Entomol. 20 (2017) 133–139, https://doi.org/10.1016/j.aspen.2016.12.006.
[59] G.L. Ellman, K.D. Courtney, V. Andres, R.M. Featherstone, A new and rapid colorimetric determination of acetylcholinesterase activity, Biochem. Pharmacol. 7 (1961) 88–95, https://doi.org/10.1016/0006-2952(61)90145-9.
[60] K. Van Asperen, A study of housefly esterases by means of a sensitive colorimetric method, J. Insect Physiol. 8 (1962) 401–416, https://doi.org/10.1016/0022-1910(62)90074-4.
[61] P.R. Penilla, A.D. Rodriguez, J. Hemingway, J.L. Torres, J.I. Arredondo-Jiménez, M.H. Rodríguez, Resistance management strategies in malaria vector mosquito control. Baseline data for a large-scale field trial against Anopheles albimanus in Mexico, Med. Vet. Entomol. 12 (1998) 217–233, https://doi.org/10.1046/j.1365-2915.1998.00123.x.
[62] T.D. Boer, J. Bruinvels, Assay and properties of 4-aminobutyric-2-oxoglutaric acid transaminase and succinic semialdehyde dehydrogenase in rat brain tissue, J. Neurochem. 28 (1977) 471–478, https://doi.org/10.1111/j.1471-4159.1977.tb10417.x.
[63] M.M. Bradford, A rapid and sensitive method for the quantitation of microgram quantities of protein utilizing the principle of protein-dye binding, Anal. Biochem. 72 (1976) 248–254, https://doi.org/10.1016/0003-2697(76)90527-3.
[64] M. Nishikimi, N.A. Rao, K. Yagi, The occurrence of superoxide anion in the reaction of reduced phenazine methosulfate and molecular oxygen, Biochem Biophys. Res. Commun. 46 (1972) 849–854, https://doi.org/10.1016/S0006-291X(72)80218-3.
[65] W.H. Habig, M.J. Pabst, G. Fleischner, Z. Gatmaitan, I.M. Arias, W.B. Jakoby, The identity of glutathione *S*-transferase B with ligandin, a major binding protein of liver, Proc. Natl. Acad. Sci. 71 (1974) 3879–3882, https://doi.org/10.1073/pnas.71.10.3879.
[66] H. Aebi, [13]Catalase in vitro, Methods Enzymol. 105 (1984) 121–126, https://doi.org/10.1016/S0076-6879(84)05016-3.

[67] E. Beutler, O. Duron, B.M. Kelly, Improved method for determination of blood glutathione, JLCM 61 (1963) 882–8881963.
[68] H. Ohkawa, N. Ohishi, K. Yagi, Assay for lipid peroxides in animal tissues by thiobarbituric acid reaction, Anal. Biochem. 95 (1979) 351–358, https://doi.org/10.1016/0003-2697(79)90738-3.
[69] R.L. Levine, D. Garland, C.N. Oliver, A. Amici, I. Climent, A.G. Lenz, B.W. Ahn, S. Shaltiel, E.R. Stadtman, [49]Determination of carbonyl content in oxidatively modified proteins, Methods Enzymol. 186 (1990) 464–478, https://doi.org/10.1016/0076-6879(90)86141-H.
[70] İ. Gulcin, Antioxidants: a comprehensive review, Arch. Toxicol. 99 (2025) 1893–1997, https://doi.org/10.1007/s00204-025-03997-2.
[71] A.A. Mohamed, E.A. Seyam, S.A. Hussein, M. Abdel-Haleem, Quercetin-mediated repression of adrA gene expression in Escherichia coli: dual roles in antibiofilm activity and oxidative stress regulation, Biologia 80 (2025) 3191–3201, https://doi.org/10.1007/s11756-025-02046-8.
[72] D. Finney, Probit Analysis, 3rd ed, 333, Cambridge Univ, Press, London, UK, 1971.
[73] A.D. Becke, Density-functional thermochemistry. III. The role of exact exchange, J. Chem. Phys. 98 (1993) 5648–5652, https://doi.org/10.1063/1.464913.
[74] S. Gavale, D. Zade, K. Patil, R. Yadav, P.R. Murumkar, R. Kadu, Synthesis, characterization, and computational insights of flavone derivatives as promising antimicrobial agents, Chem. Biodivers. 22 (2025) e02136, https://doi.org/10.1002/cbdv.202502136.
[75] M.A. Kadhim, M.G. Mukhlif, E.W. Gayadh, E.K.M. Zangana, M.A. Mohaisen, M. M. Matar, S.A. Rizk, Synthesis, design, biological activity, DFT study and molecular docking of new 1,2,4-triazine and 1,2,4-triazol derivatives bearing the phthalazine moiety, J. Mol. Struct. 1322 (2025) 140384, https://doi.org/10.1016/j.molstruc.2024.140384.
[76] T. Sharma, P. Kumari, A. Kumar, M. Ahmed, A. Ansari, Y.S. Babu, M. Brahma, M. Maruthi, A. Verma, J. Singh, B. Singh, R. Kataria, V. Kumar, Exploring biological potential of edaravone-linked pyrazoles: regioselective synthesis, anticancer, antibacterial, DNA photocleavage activity, DFT and molecular docking studies, J. Mol. Struct. 1373 (2026) 146624, https://doi.org/10.1016/j.molstruc.2026.146624.
[77] D.K. Lakhnotra, J.B. Maheta, N.H. Shaikh, I.M. Ram, Y.O. Bhola, S. Gandhi, S. B. Koradiya, Design, synthesis, and biological evaluation of Schiff base derivatives incorporating quinoline-1,2,3-triazole moieties: antimicrobial, anticancer activities, DFT simulations, and molecular docking studies, J. Mol. Struct. 1352 (2025) 144452, https://doi.org/10.1016/j.molstruc.2025.144452.
[78] A.E. Reed, L.A. Curtiss, F. Weinhold, Intermolecular interactions from a natural bond orbital, donor-acceptor viewpoint, Chem. Rev. 88 (1988) 899–926, https://doi.org/10.1021/cr00088a005.
[79] J.-i. Aihara, Reduced HOMO−LUMO Gap as an Index of Kinetic Stability for Polycyclic Aromatic Hydrocarbons, J. Phys. Chem. 103 (1999) 7487–7495, https://doi.org/10.1021/jp990092i.
[80] S. Uzun, Z. Esen, E. Koç, N.C. Usta, M. Ceylan, Experimental and density functional theory (MEP, FMO, NLO, Fukui functions) and antibacterial activity studies on 2-amino-4-(4-nitrophenyl)-5,6-dihydrobenzo[*h*]quinoline-3-carbonitrile, J. Mol. Struct. 1178 (2019) 450–457, https://doi.org/10.1016/j.molstruc.2018.10.001.